Universidad Autónoma de Nuevo León

Facultad de Ciencias Químicas

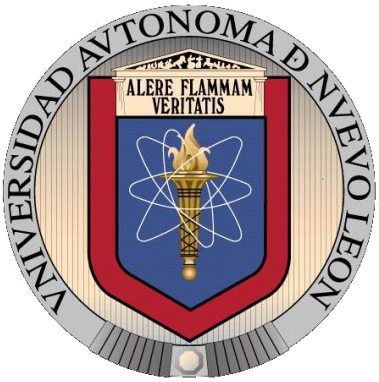

Morphology effect of silver-chitosan and gold-chitosan nanostructures on their performance in surface-enhanced Raman spectroscopy

Por

CARLOS EDUARDO PUENTE DE LEÓN

Como requisito parcial para obtener el Grado de
MAESTRO EN CIENCIAS con orientación en
Química de los materiales

Junio, 2019

Morphology effect of silver-chitosan and gold-chitosan nanostructures on their performance in surface-enhanced Raman spectroscopy

Aprobación de la Tesis:

Dr. Israel Alejandro López Hernández
Presidente

Dr. Alejandro Vázquez Dimas
Secretario

Dr. Luis Carlos Torres González
Vocal

DRA. MA. ARACELI HERNÁNDEZ RAMÍREZ
Sub-Directora de Posgrado

Morphology effect of silver-chitosan and gold-chitosan nanostructures on their performance in surface-enhanced Raman spectroscopy

Revisión de la Tesis:

Dra. Margarita Sánchez Domínguez
Co-director

Dr. Luis Carlos Torres González
Tutor 1

Dr. Alejandro Vázquez Dimas
Tutor 2

Dr. Rodrigo Chan Navarro
Tutor 3

DRA. MA. ARACELI HERNÁNDEZ RAMÍREZ
Sub-Directora de Posgrado

RESUMEN

Carlos Eduardo Puente de León Fecha de graduación: Julio, 2019

Universidad Autónoma de Nuevo León

Facultad de Ciencias Químicas

Título del estudio: MORPHOLOGY EFFECT OF SILVER-CHITOSAN AND GOLD-CHITOSAN NANOSTRUCTURES ON THEIR PERFORMANCE IN SURFACE-ENHANCED RAMAN SPECTROSCOPY

Número de páginas: 88

Candidato para el Grado de Maestro en Ciencias con Orientación en Química de los Materiales

Área de estudio: Nanoquímica

Propósito y Método del Estudio: La espectroscopía Raman aumentada en superficies es una técnica que permite la detección de una amplia variedad de sustancias a bajas concentraciones, ofreciendo una alternativa importante a los métodos convencionales de análisis. Se busca producir sustratos nuevas, de menor costo, con mayor estabilidad y biocompatibilidad para mejorar esta técnica. En este trabajo, se obtuvieron sustratos basados en nanopartículas de oro y plata con diferentes morfologías y se depositaron junto con una matriz de quitosano. Además, se analizó el efecto de la concentración del quitosano y su peso molecular sobre el desempeño Raman de los sustratos.

Contribuciones y Conclusiones: Sustratos para espectroscopía Raman aumentada en superficies basados en una matriz de quitosano sobre nanopartículas de metales nobles con morfologías específicas. Los sustratos alcanzaron límites de detección entre 10^{-4} y 10^{-9} M utilizando *p*-aminotiofenol como analito Raman.

Firma del asesor:_____

ABSTRACT

Carlos Eduardo Puente de León Graduation date: July, 2019

Universidad Autónoma de Nuevo León

Facultad de Ciencias Químicas

Work title: MORPHOLOGY EFFECT OF SILVER-CHITOSAN AND GOLD-CHITOSAN NANOSTRUCTURES ON THEIR PERFORMANCE IN SURFACE-ENHANCED RAMAN SPECTROSCOPY

Candidate for the Maestría en Ciencias con Orientación en Química de los Materiales degree

Study area: Nanochemistry

Study purpose and method: The surface-enhanced Raman spectroscopy is a technique that allows the detection of a wide variety of chemical compounds at low concentrations, offering an important alternative for commonly used methods. New and low-cost substrates with higher stability and biocompatibility are required to further enhance this technique. In this work, substrates based on gold and silver nanoparticles with different morphologies were obtained and coated with a chitosan matrix. The effect of the chitosan concentration and molecular weight on the Raman intensity enhancement was also analyzed.

Contributions and conclusions: Substrates for surface-enhanced Raman spectroscopy based on a chitosan matrix onto noble metal nanoparticles with different morphologies were developed. The substrates reached detection limits between 10^{-4} and 10^{-9} M using *p*-aminothiophenol as Raman probe molecule.

Advisor signature:_____

ACKNOWLEDGMENTS

Al Dr. Israel Alejandro López Hernández por su paciencia y apoyo durante todo este tiempo.

A la Dra. Margarita Sánchez Domínguez por su ayuda durante la realización de esta tesis.

A la Dra. Christa Brosseau, quien me aceptó en su laboratorio en Saint Mary's University, Canadá sin dudar, y me apoyó durante mi estancia de investigación.

A CONACyT por la beca otorgada.

A mi familia, por su apoyo incondicional y ayudarme a ser quien soy ahora.

A mis amigos, que si bien no los enlistaré aquí, estoy eternamente agradecido con todos ustedes.

TABLE OF CONTENTS

Chapter **Page**

TABLE LIST

Table **Page**

FIGURE LIST

Figure **Page**

NOMENCLATURE

LSPR	Localized surface plasmon resonance
UV-Vis	Ultraviolet-visible
IR	Infrared
a	Polarizability
$\boldsymbol{P}$	Electric dipole moment
$\boldsymbol{E}$	Electric field
t	Time
Q	Vibrational normal coordinate
ν_{Vib}	Material vibration frequency
I	Raman intensity
R	Detector position
θ	Detector diameter
λ	Laser wavelength
n	Refraction index
d	Particle diameter
TERS	Tip-enhanced Raman spectrometry
SERS	Surface-enhanced Raman spectroscopy

EF	Enhancement factor
HOMO	Highest occupied molecular orbital
LUMO	Lowest unoccupied molecular orbital
EC-SERS	Electrochemical surface-enhanced Raman spectroscopy
E_0	Initial electric field
λ_0	Inicial wavelength
E_{Loc}	Local electric field
E_{Scat}	Scattered electric field
E_{Rad}	Radiated electric field
λ_R	Wavelength of the Raman-shifted signal
M_{Loc}	Local enhancement factor
M_{Rad}	Radiated enhancement factor
I_{Raman}	Normal Raman intensity
I_{SERS}	SERS intensity
N_{Surf}	Number of molecules at the surface
N_{Vol}	Number of molecules at the excitated volume
M	mol/L
LOD	Detection limit
DLS	Dynamic light scattering
FE-SEM	Field-emission scanning electron microscopy
TEM	Transmission electron microscopy
rpm	Revolutions per minute

CHAPTER 1

INTRODUCTION

1.1 Plasmonic materials

The nanoparticles are materials with unique properties that differ from the ones shown by their macrometric counterparts. In the case of the metallic nanoparticles, these characteristics are produced by their plasmonic behavior at nanometric scale, which is attributed to the localized surface plasmon resonance (LSPR) of the material. The LSPR is a phenomenon caused by a coherent oscillation of the valence electrons when an electromagnetic field interacts with the metal itself; a quantum of this coherent electron oscillation is known as plasmon, and it is the base of a wide variety of emergent technologies.

The most common plasmonic materials are those composed of noble metals such as copper, silver, and gold, as their LSPR modes are in the visible and infrared light range, which is an area of interest for spectrophotometric techniques for qualitative or quantitative analysis. The wavelength of the silver and gold LSPR modes can be tuned by changing their morphology (size and shape) and chemical environment [1-3], allowing the development of materials with specific optical properties for particular applications [4-7].

Silver and gold nanoparticles are usually used with spherical morphology, showing a well-studied optical behavior: a dipolar mode at 400 nm for silver nanospheres, and a dipolar mode at 520 nm in the case of gold nanospheres. However, when the size distribution is polydisperse, the absorption band (which can be analyzed by UV-Vis spectrophotometry) is broader due to the presence of particles with different diameters. Due to the small size of the particles in this kind of dispersions, the plasmon modes are dipoles, as it can be observed in Fig. 1, thus showing only one absorption band.

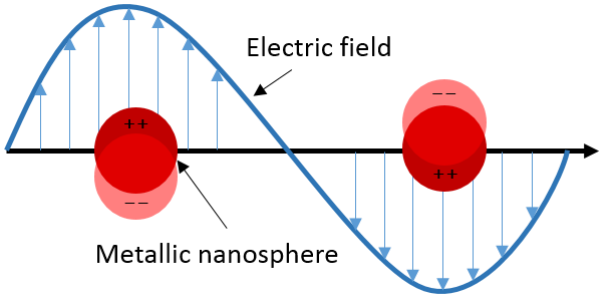

Fig. 1. Representation of the plasmon resonance of a dipolar mode produced by the incidence of an electric field on a metallic sphere.

In the case of anisotropic morphologies, such as nanorods, nanocubes, nanostars, and nanoprisms, the interactions of the incoming photons with the electron cloud of the metallic particles produces LSPR modes with complicated charge distributions. When gold nanoparticles have a rod-like morphology, two resonance modes are produced: transverse plasmon, with a maximum absorption wavelength of 520 nm; and a longitudinal plasmon, whose maximum absorption wavelength depends on the aspect ratio of the particles [8,9] The representation of these modes are shown in Fig. 2.

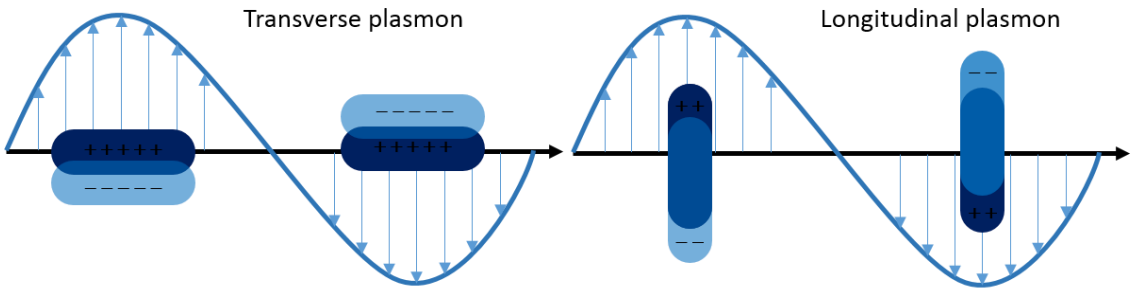

Fig. 2. Representation of the plasmon modes that can be observed on nanorods.

Although it also depends on the dielectric properties of the medium and the stabilizing agent used, the longitudinal plasmon of gold nanorods with an aspect ratio of 2 can be observed close to 630 nm; this plasmon can be tuned to longer wavelengths by increasing the aspect ratio of the particles, making the gold nanorods an interesting morphology for a wide range of uses and processes.

On the other hand, in the case of silver nanocubes, the plasmon geometry is quite complex, producing multimodal modes in which the charges are located on the corners of the cubes, on the edges, or on the facets of the particles. As mentioned before, the optical properties of the nanocubes can be tuned by modifying their size; however, in this case, the mode with the highest contribution to the final extinction behavior is different according to the size [10].

The tuning flexibility of the plasmonic nanomaterials can be used in order to develop substrates or devices for selective or enhanced detection of molecular analytes [11-13]. This is the case of using noble metal nanostructures with adjustable optical properties for enhancing the intensities of the vibrational bands detected in Raman spectroscopy, produced by the surface-enhanced Raman scattering effect [14].

1.2 Analytical determination of substances of interest

Nowadays, there is a wide variety of analytical methods and techniques for qualitative and quantitative analysis with different sensitivity and detection limit, thus allowing the detection of chemical, biological, toxic, and complex samples in more than one way. Depending on the required accuracy, time, cost, sample pre-treatment, among others.

Even with the latter, new techniques with enhanced selectivity, high reproducibility, lower cost than those commonly used, with better quantification and detection limits, and no pre-treatment or fast treatment needed, are the aim of researchers worldwide. Nevertheless, most of the existing techniques can be modified in different ways in order to obtain a better outcome; for example, using a new pre-treatment or sample preparation method, developing selective or enhancing substrates.

Among the spectroscopic techniques, Raman spectroscopy gives information about the vibrational modes of the sample, allowing its characterization and the study of different systems composed of organic molecules. Even though this technique is a powerful ally to determine the presence of specific samples and their transformations, it is not used so often due to the low intensities obtained by a normal analysis. Therefore, modifications, coupling with other techniques, and development of new substrates to address this problem is the main objective of several research projects.

1.3 Raman spectroscopy

Raman spectroscopy is a vibrational technique that allows the detection and quantification of molecular analytes by detecting the inelastic scattering (or Raman scattering) of incident light generated by a laser of a specific wavelength.

A photon excites the molecule to a virtual energy state, producing the vibration of its moieties; however, when the relaxing process occurs, the molecule ends at an excited state, thus leading to a photon with a different frequency. If the virtual energy state is higher than the initial state, scattering a photon with lower energy, we talk about a Stokes scattering; in contrast, when the final virtual energy state is lower and the photons are scattered with higher energy, an anti-Stokes scattering occurred. The probability of a Stokes scattering to occur at low temperature is higher than the probability of an anti-Stokes scattering [15]. This is represented in a Jablonski diagram, as the one shown in Fig. 3.

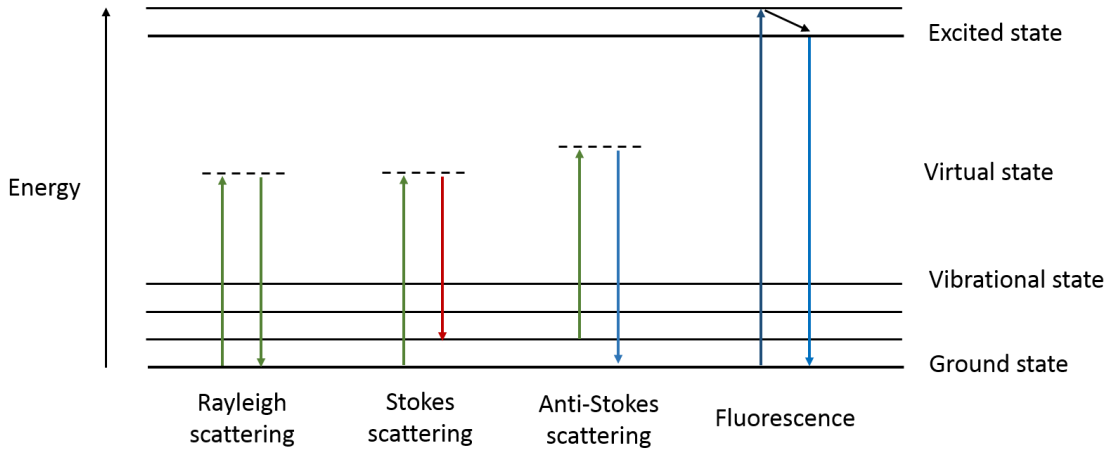

Fig. 3. Jablonski diagram showing the difference between the light interaction types.

Although infrared (IR) and Raman spectroscopies give information about the vibrational modes of the sample, these techniques are complementary and can be used for a better characterization or study of a substance. In order for the Raman effect to occur, there must be a change in the polarizability (α), which is a change in the electron cloud shape of the molecule. This is the main difference between the IR and Raman spectroscopies.

When a molecule interacts with light, an electric dipole moment (***P***) is induced according to the following equation:

$$\boldsymbol{P} = \alpha \boldsymbol{E} \tag{1}$$

this symbolizes the probability of the electronic density to be distorted by an electric field (***E***). In the case of an oscillating electric field, such as the light electromagnetic field, an oscillating electric dipole moment is induced:

$$E = E_0 cos(2\pi\nu t) \tag{2}$$

$$P = \alpha E_0 cos(2\pi\nu t) \tag{3}$$

However, **P** includes a small movement caused by the vibration of the molecule:

$$\alpha = \alpha_0 + \frac{\partial \alpha}{\partial Q} Q + \cdots \tag{4}$$

where α_0 represents the polarizability of the molecule at a static state and the second term of the equation is a correction term needed due to the vibrational movement. In this term,

Q is a vibrational normal coordinate, being Q_0 the highest position that the molecule can reach. This is calculated by the following equation:

$$Q = Q_0 \cos(2\pi \nu_{vib} t) \tag{5}$$

being ν_{vib} the vibration frequency of the material, which must not be confused with the laser frequency. Thus, the polarizability can be rewritten as:

$$\alpha = \alpha_0 + \frac{\partial \alpha}{\partial Q} Q_0 \cos(2\pi \nu_{vib} t) \tag{6}$$

and hence:

$$P = \alpha_0 E_0 \cos(2\pi \nu t) + \frac{\partial \alpha}{\partial Q} Q_0 \mathrm{E}_0 (\cos(2\pi \nu t))(\cos(2\pi \nu_{vib} t)) \tag{7}$$

If we use the trigonometric identity:

$$cos(A) \cdot cos(B) = \frac{1}{2}\{\cos(A - B) + \cos(A + B)\} \tag{8}$$

then:

$$P = \alpha_0 E_0 \cos(2\pi \nu t) + \frac{\partial \alpha}{\partial Q} \frac{Q_0 \mathrm{E}_0}{2} [\cos(2\pi(\nu - \nu_{vib})t) + \cos(2\pi(\nu + \nu_{vib})t)] \tag{9}$$

the first term of this equation represents the electric dipole moment produced by the Rayleigh scattering, whereas the other two terms represent the contribution of the Stokes scattering and anti-Stokes (respectively) scattering to the final dipole moment.

The Raman intensities of a vibrational mode can be defined by the polarizability and the collected and incident polarizations of the photons detected, as stated in the following equation:

$$I \propto |\overrightarrow{E_s} \cdot \alpha \cdot \overrightarrow{E_i}|^2 \tag{10}$$

The intensity of the light dispersed by a particle can be calculated using the detector position (R) and diameter (θ), the laser wavelength (λ), the refraction index (n) and the particle diameter (d):

$$I = I_0 \frac{1+\cos^2\theta}{2R^2} \left(\frac{2\pi}{\lambda}\right)^4 \left(\frac{n^2-1}{n^2+2}\right) \left(\frac{d}{2}\right)^6 \tag{11}$$

As the detector used in the Raman spectrometer usually can not be moved nor changed, the Raman intensity is inversely proportional to the laser wavelength:

$$I \propto \frac{1}{\lambda^4} = \lambda^{-4} \tag{12}$$

There is a wide range of lasers wavelengths that can be used for Raman spectroscopy; however, the most common are the 532, 633, 785 and 1064 nm lasers. As the laser energy depends on its wavelength, the Raman spectra obtained for the same sample is slightly different for each laser. On the other hand, changing the laser to less energetic one helps when there is a significant amount of fluorescence.

This spectrometric technique has allowed the detection of a wide variety of molecules and analytes, such as proteins, herbicides, dyes, explosives, biological compounds, among

other chemical species of interest for diseases, security, sensing, drug detection, reaction tracking and other applications [16-19].

The Raman effect can be used to get different variations of this technique such as Raman microscopy, resonance Raman spectrometry, tip-enhanced Raman spectrometry (TERS), surface-enhanced Raman spectroscopy (SERS), electrochemical surface-enhanced Raman spectroscopy (EC-SERS), among others.

Although this technique is powerful and useful, the intensities detected in a regular Raman spectroscopy analysis are very low, leading to difficulties in the quantification of a sample or species. Surface-enhanced Raman spectroscopy (SERS) is a technique derived from the Raman spectroscopy, in which a nanoparticle-containing substrate is used to enhance the intensity of the normal Raman vibrational modes of the sample; such intensities increase can reach enhancement factors (EF) as high as 10^6.

1.4 Surface-enhanced Raman scattering and spectroscopy

In 1974, Fleischma, Hendra, and McQuillan reported the pyridine Raman analysis using a roughened silver electrode as substrate [20]; however, the high intensities of the Raman bands were not discussed by the group. A few years later, Van Duyne and Jeanmaire tried to explain this behavior with a spectroelectrochemical point of view [21]. It was until 1978 when Van Duyne and Schatz published a paper proposing an electromagnetic theory that explains this unusual increase: a change in the polarizability derivate of the molecule due to the image produced on the electrode surface [22]. Independently, in the same year, Moskovits proposed that the produced intensity enhancement on Ag and Cu were caused by a pre-resonance of the LSPR at the roughened

electrode surface [23]. It was after the discovery of Fleischmann that the studies of systems and analytes using SERS began its exponential growth that prevails until now.

Even though the mechanism that produces the surface-enhanced Raman scattering effect is still under debate, two mechanisms that work simultaneously to produce a high increase are now widely accepted by the scientific community: the chemical, or charge-transfer, theory, and the electromagnetic theory [24].

1.4.1 Charge-transfer enhancement mechanism

In the case of the charge-transfer enhancement, the molecule must be adsorbed directly onto the substrate surface. This occurs usually with molecules with lone electron pairs, thus making it possible to increase this effect by applying an electric potential. In the system, the energy obtained from the incoming photons is enough to allow an electronic transfer from the highest occupied molecular orbital (HOMO) of the molecule to the Fermi level of the metal [25,26]. Also, the case of an electron transfer from the Fermi level to the lowest unoccupied molecular orbital (LUMO) of the molecule is a second type of charge-transfer mechanism. Fig. 4 represents the charge-transfer mechanism. This enhancement has a great importance in EC-SERS.

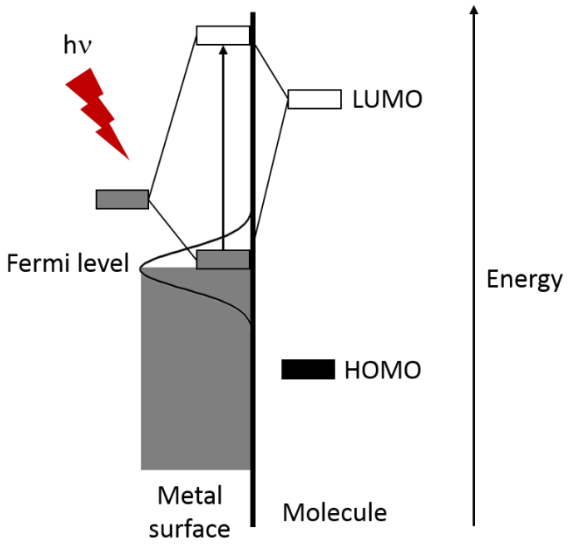

Fig. 4. Scheme of the charge-transfer SERS enhancement mechanism.

1.4.2 Electromagnetic enhancement mechanism

In contrast, a direct bond between the molecules and the metal is not required in the electromagnetic mechanism; nevertheless, the analytes must be close to the metal nanoparticles of the substrate [14]. As the photons interacts with the plasmonic nanoparticles with an initial electric field (E_0) and a wavelength (λ_0), the localized surface plasmons are excited, producing an increased local electric field (E_{Loc}) around the nanoparticles:

$$E_{Loc} = M_{Loc}\lambda_0 E_0 \tag{13}$$

As the analyte enters into the vicinity of the particle, the local field polarizes the molecule, producing Raman scattering. However, a new electric field has been created: the scattered electric field (E_{Scat}), which is proportional to E_{Loc} and the polarizability of the molecule:

$$E_{Scat} = \alpha E_{Loc} \tag{14}$$

As a second step, E_{Scat} will interact with the nanoparticle thus producing the radiated electric field (E_{Rad}), which is proportional to E_{Scat} and the wavelength of the Raman shifted signal (λ_R):

$$E_{Rad} = M_{Rad}\lambda_R E_{Scat} \tag{15}$$

hence:

$$E_{Rad} = \alpha M_{Loc}\lambda_0 M_{Rad}\lambda_R E_0 = E_{SERS} \tag{16}$$

where M_{Loc} and M_{Rad} are enhancement factors that are wavelength-dependent. Finally, the SERS intensity can be described as a function of the enhancement factors and the Raman intensity (I_0):

$$I_{SERS} = M_{Loc}^2\lambda_0 M_{Rad}^2\lambda_R I_0 \tag{17}$$

As the Raman shift is low, the incident and Raman-shifted wavelengths are close between each other, and can be used as the same value; the latter also occurs with the enhancement factors. This leads to:

$$I_{SERS} \approx M_{Loc}^4\lambda_0 I_0 \tag{18}$$

this equation represents that the SERS intensity is approximately the forth power of the enhanced electric field near the nanoparticle, proving the huge importance of the electric

field created near the nanoparticles at the SERS substrate [27,28]. This enhancement mechanism is shown in Fig. 5.

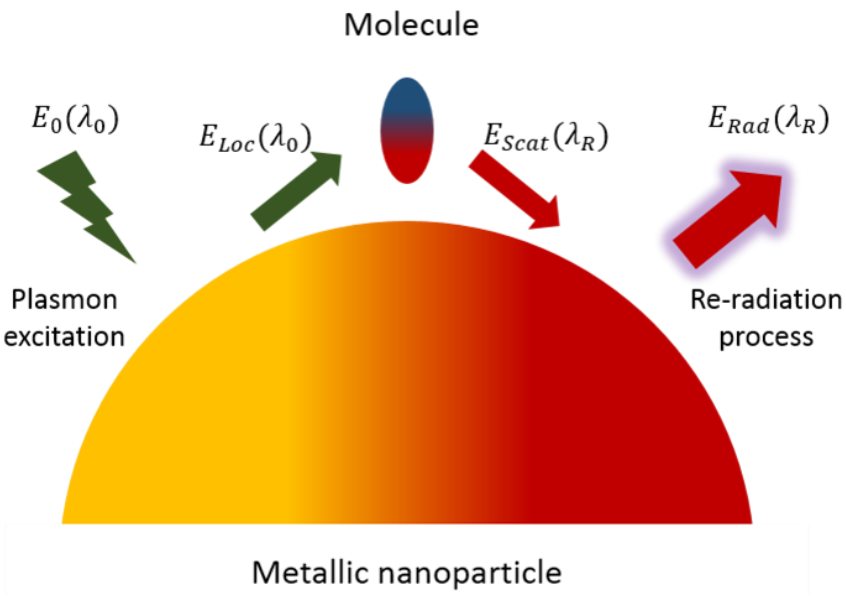

Fig. 5. Electromagnetic SERS enhancement mechanism diagram.

1.4.3 Enhancement factor

In order to compare conventional Raman spectroscopy and SERS, researchers defined a term known as enhancement factor, which can be calculated theoretically with the enhanced electric fields. However, the theoretical EF is not as useful as the experimental EF obtained; thus, an expression involving the Raman (I_{Raman}) and SERS (I_{SERS}) intensities, the number of molecules at the surface (N_{Surf}) of the SERS substrate, and the number of molecules in the excitation volume (N_{Vol}) is often used.

$$EF = \frac{I_{SERS}/N_{Surf}}{I_{Raman}/N_{Vol}} \tag{19}$$

The EF that can be achieved by the charge-transfer mechanism is in the range of 10 and 10^6, depending on the adsorbed molecule nature [29]. In contrast, the EF that can be reached with the electromagnetic field mechanism are in the order of 10^7.

On the other hand, when the system is composed of plasmonic nanoparticles with spikes or edges, such as nanostars and nanocubes, the highest electric field increase occurs at the ends of those spikes and edges. In addition, when the substrate is an array of particles, the gaps between them produce hot spots, which are regions where the electric field was greatly enhanced [30]. These cases offer areas where the electromagnetic mechanism can lead to huge EF values.

Nevertheless, uniform substrates based on anisotropic nanostructures are hard to prepare by mild or low-costed methods, and they show low selectivity and biocompatibility. Some methods reported for the obtainment of SERS substrates are island lithography, electrospinning, chemical synthesis, self-assembly, etching, among others [31-33].

An alternative to this problem is the use of biopolymers as a support matrix for the plasmonic nanoparticles. This will allow the production of SERS substrates by low-cost procedure, with good particle distribution along the substrate, and a higher affinity to biological analytes and samples. Some biopolymers used for SERS are pectin [34], gelatin [35], chitosan [36], chitin [37], among others.

1.5 Chitosan

Chitosan (CS) is a polysaccharide with linked β-(1,4) D-glucosamine and *N*-acetyl-D-glucosamine units, and it can be prepared by partial deacetylation of the chitin obtained from fungi cell walls and crustaceans' shells such as *Pandalus borealis*. This biopolymer is known for its biocompatibility and the possibility of being used for drug, genes, and protein delivery [38]. Its structure is shown in Fig. 6.

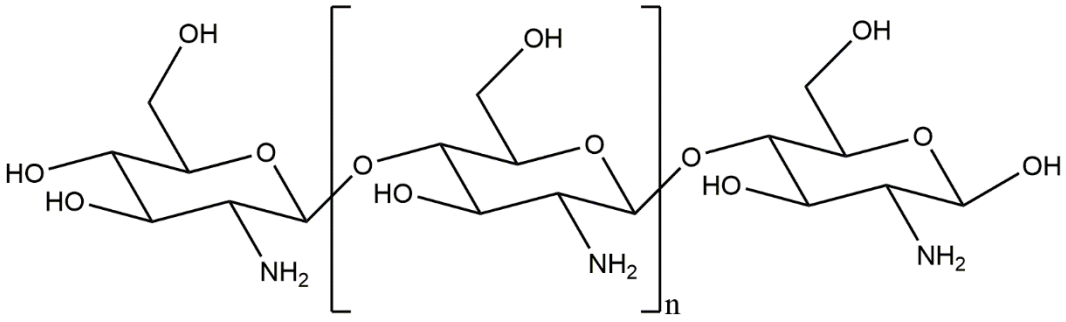

Fig. 6. Representation of the chitosan chemical structure.

The physical and chemical properties of this biopolymer allow its use as capping agent for the synthesis of biocompatible, environmentally friendly and non-toxic noble metal nanostructures [39]; however, when the used stabilizing agent is chitosan, the nanoparticles obtained show usually a spherical or triangular shape. On the other hand, the biocompatibility of chitosan-capped nanoparticles, when applied to SERS analysis, allows the detection of biological species of interest such as proteins, explosives, drugs, antibiotics, among others [40-44].

CHAPTER 2

BACKGROUND

This chapter focuses on the previous works that helped in the design and development of this research project.

In 2012, Murray *et al*. published a methodology for the obtainment of Au nanorods with a lower surfactant concentration when compared to well-established synthesis procedures [45]. In this work, the nanoparticles were obtained by the addition of aromatic additives. These nanorod dispersions showed different aspect ratios according to the aromatic molecule used, and therefore, this synthesis allows the adjustment of the Au nanorod longitudinal plasmon band between 600 and 1200 nm.

The synthesis of star-like Au nanostructures functionalized with 1-dodecanethiol obtained using ascorbic acid (AA) as reducing agent and cetyltrimethylammonium bromide (CTAB) as stabilizing agent was reported in 2015 by de la Rosa *et al*., and used for the fabrication of SERS substrates [46]. The tips of the nanostar array in the silicon and silicon/Au substrates led to the formation of hot spots, which allowed the achievement of EF in a range of 10^7 and 10^9 with a detection limit (LOD) between 10^{-9} and 10^{-14} M when detecting rhodamine B (RhB), *p*-terphenyl and tween 20.

In a similar way, in 2016, Xia *et al.* reported a procedure for the synthesis of Ag nanocubes with sharp edges using cetyltrimethylammonium chloride (CTAC) as stabilizer and AA as reducing agent [47]. The authors used the nanocubes dispersion for the SERS detection of 1,4-benzenedithiol obtaining an EF of $1.34x10^5$ and a LOD of 10^{-6} M; however, the probe molecule and the nanoparticles were mixed before the SERS analysis, and thus, ready-to-use substrates were not fabricated.

Ag nanowires synthesized in ethylene glycol (EG) using poly(vinylpyrrolidone) (PVP) as stabilizer and its use for SERS, were reported in 2014 by Zhou *et al.* [48]. A LOD of 10^{-8} M and an EF of $1.2x10^7$ were achieved when using these nanowires for the detection of crystal violet (CV); this EF value allowed the use of these nanostructures for the determination of the thiram pesticide with a LOD of $1x10^{-7}$ M. However, once again, the SERS substrates were prepared by depositing a mixture of the analyte solution and the nanowire dispersion on glass and simply let it dry.

As mentioned before, chitosan has been used for the stabilization of Ag and Au nanoparticles thanks to its amine moieties that allow electrostatic stabilization. In 2014, Wang *et al.* reported the use of chitosan-stabilized Au nanoparticles for the fabrication of an electrochemical sensor for kanamycin antibiotic [49]. In this work, the authors reacted a chitosan solution in acetic acid with $HAuCl_4$ and KBH_4 and obtained sphere-like nanoparticles embedded on a chitosan matrix. Nevertheless, only nanosphere-like structures were synthesized; also, the authors did not analyze the SERS effect of the obtained material.

Similarly, chitosan-functionalized Au nanoparticles were used by Kraatz *et al*. in 2015 for the modification of a glass carbon electrode for electrochemical detection of *Salmonella* cells [50]. During this research, Au nanoparticles are first obtained by the reduction of $HAuCl_4$ in presence of citrate ions; a further functionalization of the nanoparticles is achieved by the direct addition of a chitosan solution into the Au nanoparticle dispersion. The results showed small spherical nanoparticles on a chitosan matrix. Once again, only sphere-like morphologies were obtained, and no SERS study was performed.

In 2014, Veerabhadram *et al.* reported a one-step hydrothermal synthesis procedure for the obtainment of Ag nanoparticles with chitosan as stabilizing agent; however, the material was used for catalysis and antimicrobial evaluations [51]. For this synthesis, the direct hydrothermal reaction of a chitosan and Ag nitrate solutions led to the formation of aggregated sphere-like structures with a wide size dispersion. This study showed the synthesis of polydispersed Ag nanospheres at higher pressure and temperature than the atmospheric conditions. Although this material is suitable for SERS, the authors did not analyze this behavior.

Noble metal-chitosan nanostructures have been used for the fabrication of SERS substrates. To the best of our knowledge, the reports regarding noble metal-chitosan composites for SERS detection or analysis are shown in Table 1, where information of the nanostructure and probe molecule used, as well as the obtained LOD and EF (if they are mentioned in the paper), can be observed.

Table 1. Chitosan-covered nanostructures used in SERS, and their LOD and enhancement factor reported in the literature.

Metal	Morphology	Probe molecule	LOD	EF	Reference
Ag	Triangular nanoplates	Adenine	$12x10^{-6}$ M	**NA	36
Ag	3D hybrid porous nanostructures	RhB	10^{-5} M	$6.7x10^{4}$ for RhB	41
Au/Ag	Nanopopcorn	Melamine	10^{-8} M	Not reported	42
CS/Au/ graphene oxide	Spheres decorated graphene	Antibiotics and drugs	$10^{-4} – 10^{-8}$ M	Not reported	43
Ag	Ag/CS@SiO_2 nanospheres	Cytochrome b5	$2x10^{-5}$ M	1200	44
Ag	Nanospheres	CV	100 ppm	*Approx. 130	52
Au	Nanoflowers	2-chlorothiophenol	10^{-4} M	*Approx. 23	53
Ag	Nanospheres	R6G	$2x10^{-5}$ M	$1x10^{8}$	54
Au	Nanospheres	CV, R6G, IR-820, Nile blue chloride	10^{-6}, 10^{-5}, 10^{-5}, 10^{-7} M	$1x10^{7}$	55
Au	Nanospheres	R6G	$2x10^{-6}$ M	Not reported	56
Au	Nanospheres	R6G	10^{-8} M	Not reported	57
Ag	Nanospheres	*p*-aminothiophenol (*p*-ATP), platelet-derived growth factor BB	10^{-4} M and 10 pg/mL	Not reported	58
Au	Nanoseeds	Dopamine	10^{-3} M	Not reported	59
Ag	Triangular nanoplates	p-ATP	10^{-3} M	Not reported	60
Ag	Nanospheres and Triangular nanoplates	p-ATP	10^{-5} M	**NA	61
Au	CS/Au Core-shell nanospheres	Dopamine	10^{-3} M	*Approx. 100	62
Au	Nanosphere-like	Methylene blue and paracetamol	10^{-6} and 10^{-3} M	**NA	63
CS/Ag	Decorated nanowires	RhB	10^{-5} M	*Approx. 3	64
Au/Ag	Nanoflowers	Cresyl violet	10^{-6} M	$3x10^{6}$	65
Au	Spherical nanoshell	γ-aminobutyric acid	$15x10^{-3}$ M	Not reported	66
Ag	Dendrites	4-aminobenzenethiol	10^{-6} M	**NA	67

Table 1. Chitosan-covered nanostructures used in SERS, and their LOD and enhancement factor reported in the literature. (Continued)

Au	Nanospheres	R6G	10^{-4} M	Not reported	68
Au	Nanospheres and triangular nanoplates	L-tryptophan	10^{-3} M	**NA	69
Ag	Nanospheres	Tricyclazole and sudan I	50 ppb and 10 ppm	7.12	70
Au	Nanoflower	Polypyrrole	$5x10^{-2}$ ppm	*Approx. 9	71
Ag	Nanosphere-like	Adenine	10^{-6} M	$1x10^{4}$	72
CS/poly (ethylene oxide) /Au	Nanospheres on fibers	2-naphthalenethiol	10^{-12} M	$2x10^{5}$	73
CS/poly (ethylene oxide) /Ag	Nanospheres on fibers	RhB and *Escherichia coli* cells	10^{-5} M and $1.5x10^{9}$ cell/mL	174	74
Ag	Nanosphere-like	Nile Blue A, methidathion, isocarbophos, triazhopos, R6G	10 ppt, 100 ppm, 100 ppm, 100 ppm, 10 ppm	Not reported	75

*Value calculated with the Raman and SERS intensities shown in the papers.
**The solid analyte Raman spectrum was compared with an analyte solution SERS spectrum at a specific concentration.

Among all works shown in the previous table, an important research is the one published by Chang *et al.* in 2012 [54], in which chitosan-stabilized Ag nanoparticles were obtained by a photochemical UV-light irradiation procedure on a Au substrate. The fabricated SERS substrate composed of spherical nanoparticles was incubated in a $2x10^{-5}$ M R6G solution for the analysis. The authors achieved a LOD of $2x10^{-5}$ M and a high EF value of $1x10^{8}$. However, these substrates fabrication require a Au inert substrate, which is an expensive material. On the other hand, this is the highest EF achieved to the date for noble metal-chitosan nanostructures.

In a similar way, the synthesis of chitosan-modified popcorn-like Au nanoparticles and the evaluation of their SERS properties was published in 2015 by Hu *et al.* [42]. The

chitosan/popcorn-like structures were obtained by a simple Au(III) reduction in presence of chitosan, Ag(I) and AA; this dispersion was then used for the detection of melamine in milk powder in a capillary tube, showing a LOD of 10^{-8} M. Although this project proves the possibility of detecting biological species from real samples at low concentrations, the EF value is not reported for this dispersion; also, the SERS measurements were performed as a dispersion and not as an analyte deposited on a nanostructured substrate.

Au-Ag nanoflowers encapsulated in chitosan were synthesized in 2015 by Hu *et al.* [65], and also used for the SERS imaging of living cells. The flower-like nanostructures were obtained by the reduction of Au(III) in presence of chitosan, Ag(I) and AA. In this case, the chitosan polymer acts as an encapsulating agent that provides stability to the nanoparticles. The SERS characteristics of this dispersion were evaluated using a 1 mM cresyl violet solution as probe analyte, showing an analytical EF of $3x10^6$; however, this molecule was added during the obtainment of nanostructures. As this project focuses on the cells imaging, using these nanoparticles for different analyte detection is not easy as the molecules must be in the system as the nanoparticles are synthesized; on the other hand, the EF reported, with a value of $3x10^6$, can be compared with commercialized SERS substrates.

2.1 Critical analysis

By analyzing the published literature, there are many reports about the obtainment of different noble metal nanoparticle morphologies by a wide variety of methods; some of them include the use of chitosan polymer as capping or functionalizing agent for the final nanostructure. In addition, the presence of this polymer provides biocompatibility and

environmentally friendly characteristics that allow their use in medicine, food industry, as well as sensor development of important biological samples.

At the same time, the noble metal nanostructures produce the SERS phenomenon that allows the detection of different analytes at low concentrations. Among them, anisotropic morphologies with tips or peaks often show high EF due to the formation of hot spots. The highest EF achieved by noble metal-chitosan nanocomposites until now is $1x10^8$, whereas the LOD depends on the analyte used for the analysis, with a reported general LOD range between 10^{-3} to 10^{-8} M. However, in most of the works, the addition of the analyte probe is performed during the synthesis of the nanocomposite or before the deposition of the material on a suitable substrate; although this maximizes the interactions between the probe and the particles, leading to higher intensities, this procedure also avoids the fabrication of ready-to-use SERS substrates based on the nanocomposites. Ready-to-use substrates show some advantages such as becoming a product that can be commercialized, which expands its use to non-plasmonic research groups; also, the results obtained by these substrates can be compared when used to detect different analytes.

In addition, not all of the works report the EF value obtained nor the used solution concentrations that allow an adequate comparison of the different SERS substrates reported. Because of the latter, it would be hard to choose a selective and suitable substrate for a professional with no experience in the field of plasmonics.

As mentioned before, shapes with edges tend to cause larger electromagnetic field enhancement, leading to higher SERS intensities; however, when chitosan is used for the stabilization of noble metal nanoparticles, spherical or triangular shapes are often

obtained. This opens the possibility of producing better substrates with a biopolymeric matrix; nevertheless, there are no studies about the nanoparticle morphology effect of chitosan-containing substrates on the Raman intensity enhancement.

2.2 Hypothesis

The silver-chitosan and gold-chitosan nanostructures with specific morphologies allow the detection of *p*-ATP at 10^{-6} M by surface-enhanced Raman spectroscopy.

2.3 General objectives

Fabrication of silver-chitosan and gold-chitosan substrates with specific morphologies and evaluation of their SERS performance.

2.4 Specific objectives

- To synthesize Ag and Au nanoparticles with different morphologies.
- To characterize the noble metal nanoparticles by optical and microscopic techniques such as UV-Vis Spectrophotometry, Dynamic Light Scattering (DLS) Field-Emission Scanning Electron Microscopy (FE-SEM) and Transmission Electron Microscopy (TEM).
- To deposit the metallic nanoparticles onto an aluminum substrate.
- To deposit chitosan with low, medium or high molecular weight onto the nanoparticle substrates.
- To characterize the silver-chitosan and gold-chitosan nanostructures by structural, optical and microscopic techniques such as X-ray photoelectron spectroscopy (XPS), Raman spectroscopy, FE-SEM, and TEM.

- To evaluate the detection limit and/or enhancement factor of the materials when used as SERS substrates.

CHAPTER 3

MATERIALS AND METHODS

3.1 Synthesis of silver nanospheres (AgNS)

The Ag nanospheres were obtained by using a synthetic method previously reported by the research group [76]. In this procedure, 30 mL of 5 mM trisodium citrate (Na_3Cit) solution were added to 59 mL of deionized water and mixed with 10 mL of 1 mM $AgNO_3$. Finally, 1 mL of 8 mM $NaBH_4$ solution was added dropwise under stirring conditions; a color change from colorless to yellow was observed.

3.2 Synthesis of silver nanocubes (AgNC)

For the obtainment of sharp-edged Ag nanocubes, we followed the synthesis protocol reported by Xia *et al.* [47]. For this synthesis, 50 mL of 20 mM CTAC and 5 mL of 0.1 M AA were added in a flask and heated at 60 °C for 10 min. The pH value of the solution was then adjusted to 3.1 with NaOH or HCl as required, and then, 500 μL of 10 mM CF_3COOAg and 1 mL of 4.29 μM $FeCl_3$ were added quickly to the system and let react for 4 h under room light conditions. After 4 h, the yellow-green dispersion was purified by centrifugation at 4000 rpm for 20 min and then redispersed in water.

3.3 Synthesis of gold nanospheres (AuNS)

To synthesize spherical Au nanoparticles, we used a procedure previously reported by the research group [77]. During this procedure, 50 mL of 0.25 mM $HAuCl_4$ were heated until the solution boiled, then 2.5 mL of a 10% w/v Na_3Cit solution were added and left heating for 20 min. The final dispersion was ruby red colored.

3.4 Synthesis of gold nanorods (AuNR)

The synthesis method used for the obtainment of Au nanorods is based on the work reported by Murray *et al.* [45]. First, a seed solution was prepared by mixing 1 mL of 0.5 mM $HAuCl_4$, 1 mL of 0.2 M CTAB, and 200 μL of 6 mM $NaBH_4$ while stirring at 1000 rpm. This seed solution was aged for 30 min at room temperature before its use.

For the preparation of the growth solution, 0.0961 g of sodium 3-methylsalicylate (S3MS) were dispersed in 10 mL of warm water and let react with 0.025 g NaOH until all of the powder was dissolved. 0.990 g of CTAB and 15 mL of warm water were added to the previous solution. 0.6 mL of 4 mM $AgNO_3$ were added after the solution got cool, and then it was aged for 15 min. Afterwards, 25 mL of 1 mM $HAuCl_4$ were added to the aged solution and let react for 15 min before the addition of 0.1 mL of 0.064 M AA. The solution was vigorously stirred until colorless.

For the nanorods growth, 80 μL of the seed solution were added to the growth solution while vigorously stirring. After 1 min, the mixed solution was aged for 12 h. The nanoparticles purification was achieved by centrifugation at 8000 rpm for 20 min.

3.5 Preparation of nanoparticle pastes

For the preparation of the AgNC, AuNS and AuNR pastes, each dispersion was centrifuged for 20 min at a suitable speed (8000 rpm for AuNR, 6000 rpm for AuNS, and 4000 rpm for AgNC) and the supernatant was removed with a micropipette. For the AgNS paste, the dispersion must be concentrated by solvent evaporation before centrifuging at 8000 rpm for 20 min, and the pellet was transferred to another Eppendorf tube; after all of the pellets were collected, this new nanoparticle concentrate was centrifuged at the same conditions and the supernatant removed.

In the case of the AuNR, the resulting pellet was used as the paste, whereas in the case of the other dispersions, water was added until a final volume (40 μL for AuNS, 25 μL for AgNS, and 20 μL for AgNC). The pastes were kept under darkness until their further use.

3.6 Nanoparticles characterization

The obtained noble metal nanostructures were characterized by means of UV-Vis Spectrophotometry, DLS, FE-SEM, and TEM. The UV-Vis spectra were recorded using a Shimadzu UV-1800 spectrometer, the DLS equipment was a Zetatrac NPA152 Microtrac analyzer. In order to perform an X-ray diffraction (XRD) analysis, a Bruker D2 Phaser was used. Two FE-SEM instruments were used: a Tescan Mira 3 microscope at 20 kV) and a secondary electron detector (used to image the AgNC dispersion and all of the substrates, and a FEI Nova NanoSEM 200 at 15 kV and a Helix detector (used to image

the AgNS, AuNS, and AuNR dispersions). The TEM microscope used was a FEI Tecnai 12 in bright field mode and 80 kV.

3.7 SERS substrates fabrication, characterization, and measurements

For the preparation of SERS substrates, a drop-casting procedure was followed. For the AuNS and AgNS substrates, 2.0 μL of the nanoparticles paste was deposited on a polished aluminum (Al) substrate located in a Petri dish with water, and it was allowed to dry with the dish closed. Similarly, for the AgNC and AuNR substrates, 2.0 μL of paste was added onto a polished Al substrate and let dry under normal conditions. Subsequently, 2.0 μL of a 0.125% w/v chitosan solution in 1% v/v acetic acid was deposited onto the nanoparticle film and let dry. In a similar way to the nanoparticle dispersion, the chitosan-modified substrates were characterized by FE-SEM.

For the SERS measurements, 2.0 μL of 1 mM *p*-aminothiophenol (*p*-ATP) was deposited on the fabricated substrates and let dry. All Raman spectra were performed in a benchtop Delta Nu Advantage 785 spectrometer with a 785 nm laser, at a power of 2.15, 12.17, 26.67 or 38.77 mW, and 10 s as integration time. In order to analyze the impact of the chitosan concentration on the SERS effect, substrates with no chitosan, chitosan at 0.125% w/v and chitosan at 0.250% w/v were studied. On the other hand, the effect of the chitosan molecular weight was evaluated by the analysis of substrates made this polymer at low, medium, and high molecular weight at a concentration of 0.125%.

In order to determine the detection limit of the substrates, Raman spectra of *p*-ATP at different concentrations were recorder. The analyte concentrations analyzed were 10^{-3} to

10^{-9} M; however, the analyte was also analyzed at 10^{-2} M for the obtainment of the conventional Raman intensity, required for the calculation of the EF.

CHAPTER 4

RESULTS AND DISCUSSION

4.1 Nanoparticle characterization

The optical properties of the obtained nanoparticle dispersions were characterized by means of UV-Vis spectroscopy in order to determine the LSPR modes wavelength; also, DLS, FE-SEM and TEM were used to characterize the size, shape and size distribution of each dispersion.

4.1.1 Silver nanospheres (AgNS)

Fig. 7 shows the UV-Vis spectrum of the AgNS dispersion. This spectrum shows an absorption band with a maximum at 410 nm, which is characteristic of the LSPR of Ag nanoparticles with spherical shape. The absorption wavelength of this dipolar plasmon leads to the yellow color that can be observed by this dispersion [78].

The DLS analysis can be observed in Fig. 8. The results obtained from this technique suggest the presence of nanoparticles with a hydrodynamic diameter between 25 and 40 nm. This technique calculates the size of a hard sphere with the same translational diffusion coefficient as the particles measured, along with the electrical double layers around the particle itself; and thus, these results indicate a dispersion composed by nanospheres with a smaller size.

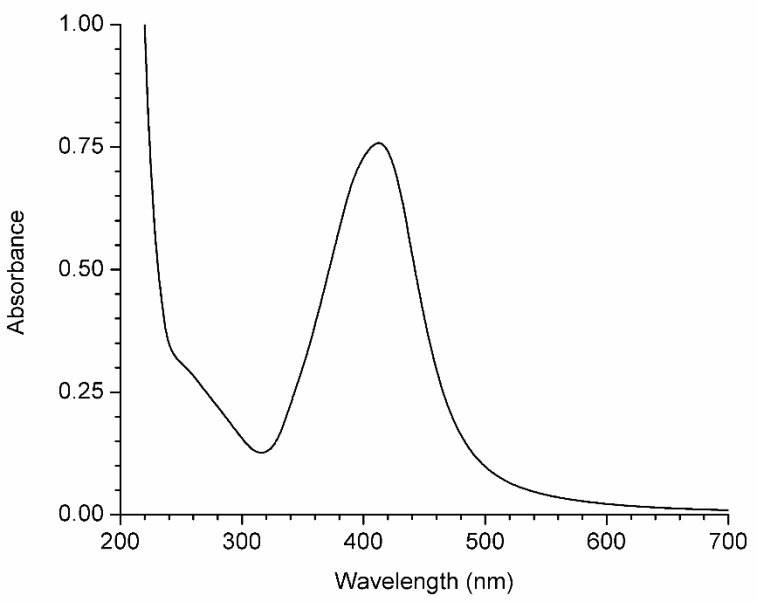

Fig. 7. UV-Vis spectrum of the Ag nanosphere dispersion.

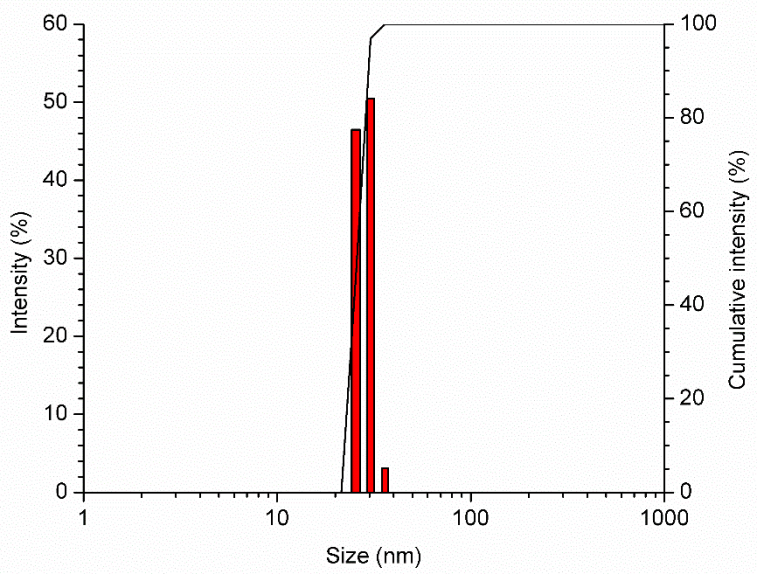

Fig. 8. DLS analysis of the Ag nanospheres colloidal dispersion.

The FE-SEM micrographs obtained for AgNS shows spherical nanoparticles with an average diameter of 10.3 ± 1.2 nm, as it can be observed in Fig. 9. In this micrograph, it can be observed that the particles are contained in an organic matrix. This matrix is sodium citrate, a residue of the synthesis procedure. Additionally, a size distribution histogram

obtained by image analysis of 60 particles using the software ImageJ, shows that the nanoparticles are in diameter range between 5 and 17 nm.

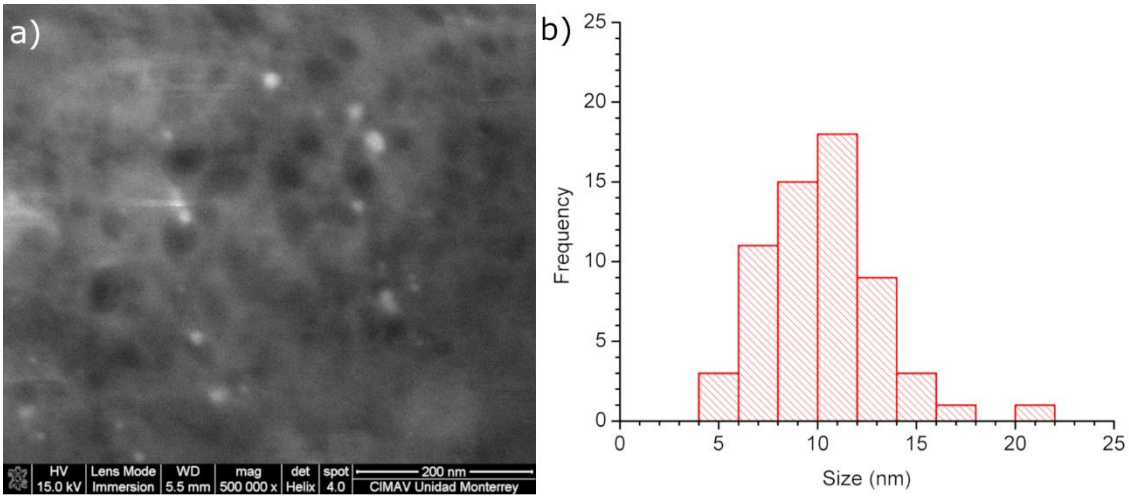

Fig. 9. a) FE-SEM micrograph of the Ag nanospheres, and b) size distribution histogram obtained by image analysis of the micrograph.

On the other hand, a TEM analysis was performed in order to correctly analyze the nanoparticle morphology. As observed in Fig. 10, the dispersion is composed of sphere-like particles in a diameter range of 3 – 14 nm and an average diameter of 7 ± 1.8 nm. Due to the higher resolution of this technique, it is possible to visualize the presence of Ag seeds, which lead to a polydisperse dispersion. These results confirm the DLS and FE-SEM results previously shown.

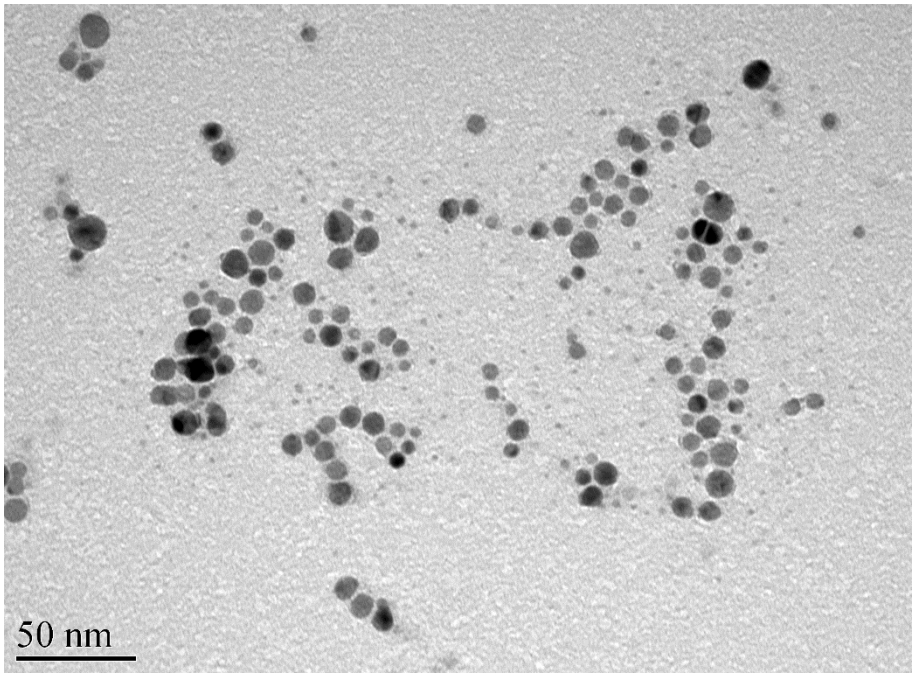

Fig. 10. TEM micrograph of the Ag nanospheres dispersion.

4.1.2 Silver nanocubes (AgNC)

As the first step of the AgNC involves the formation of AgCl octahedra, followed by a photoreduction process and posterior nanocube growth [47], XRD analysis was performed to discard the obtainment of AgCl nanoparticles. This diffractogram is shown in Fig. 11. The characteristic reflexions of zero-valent Ag (as indicated by the PDF reference, No. 00-004-0783) confirms the obtainment of Ag^0 nanoparticles.

On the other hand, Fig. 12 shows the UV-Vis spectrum of the AgNC dispersion. Absorption bands at 352, 390, and 468 nm can be observed in this spectrum, which are consistent with the characteristic LSPR complex modes for nanocubes [10]. As the optical properties of the Ag nanocubes are size-dependent, the analysis of the absorption bands may lead to the approximate size of the particles. By comparing the UV-Vis spectrum

obtained in this work and the reported spectra, we may conclude that the synthesized nanoparticles have an average size close to 56 nm [47].

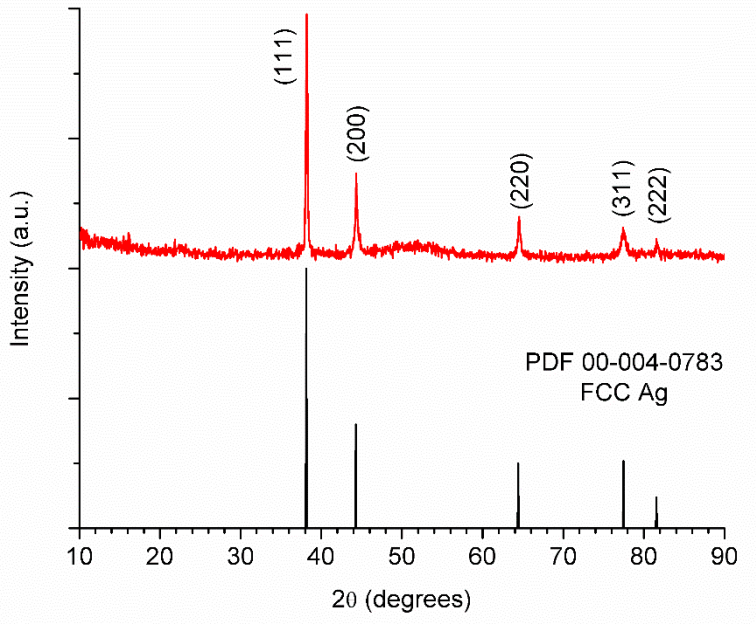

Fig. 11. X-ray diffractogram of the obtained Ag nanocubes dispersion and a reported FCC Ag diffractogram (PDF 00-004-0783).

The DLS analysis of this dispersion, presented in Fig. 13, shows the presence of particles in a size distribution range close to 150 and 170 nm. According to the size prediction that can be obtained by analyzing the UV-Vis spectrum, these results may be caused by clusters of a few nanocubes and their stabilizing agent layers.

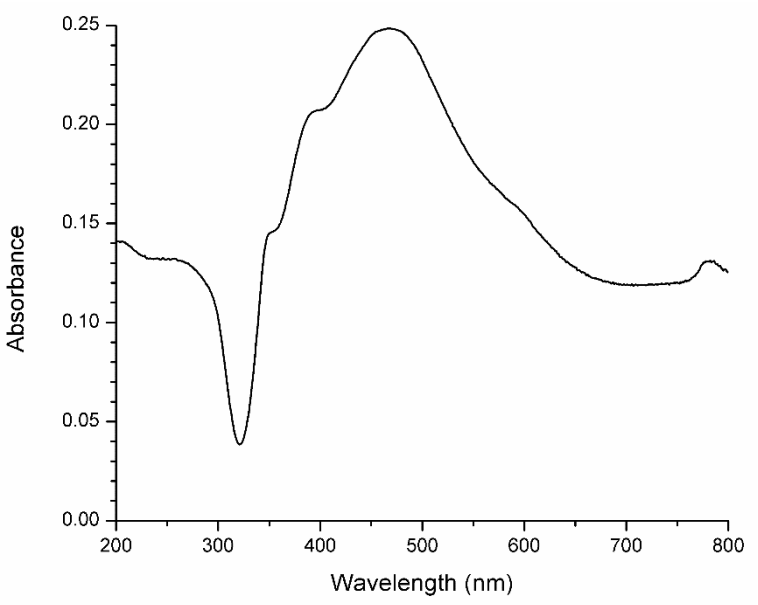

Fig. 12. UV-Vis spectrum of the Ag nanocubes dispersion.

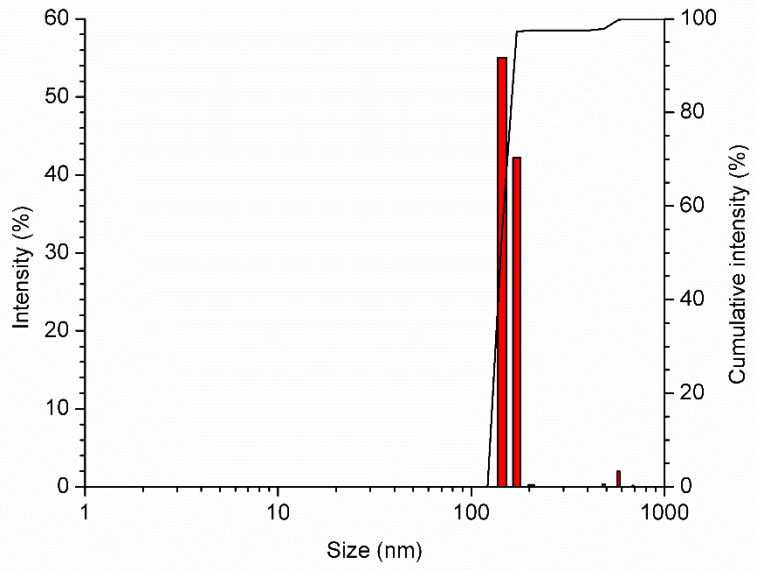

Fig. 13. DLS analysis of the Ag nanocubes colloidal dispersion.

A FE-SEM analysis was performed in order to characterize the morphology of the synthesized dispersion. The micrographs, presented in Fig. 14, show cubic nanoparticles with slightly rounded edges and an average size of 54 ± 5.7 nm; however, about 30% of the particles include additional shapes such as nanowires and nanoprisms. The presence

these additional structures can affect the UV-Vis behavior previously mentioned; however, the highest UV-Vis bands of silver nanowires (which is the second abundant morphology) are usually observed at 380 and 410 nm, depending on the wire length [79]. Due to this and the low nanowire concentration in the dispersion, minor or no contribution of these particles to the optical properties can be assumed. This morphological analysis confirms the results obtained by UV-Vis spectroscopy about the nanocubes average size. Also, a size distribution histogram obtained by image analysis of 86 particles shows a nanoparticle size range between 41 and 67 nm.

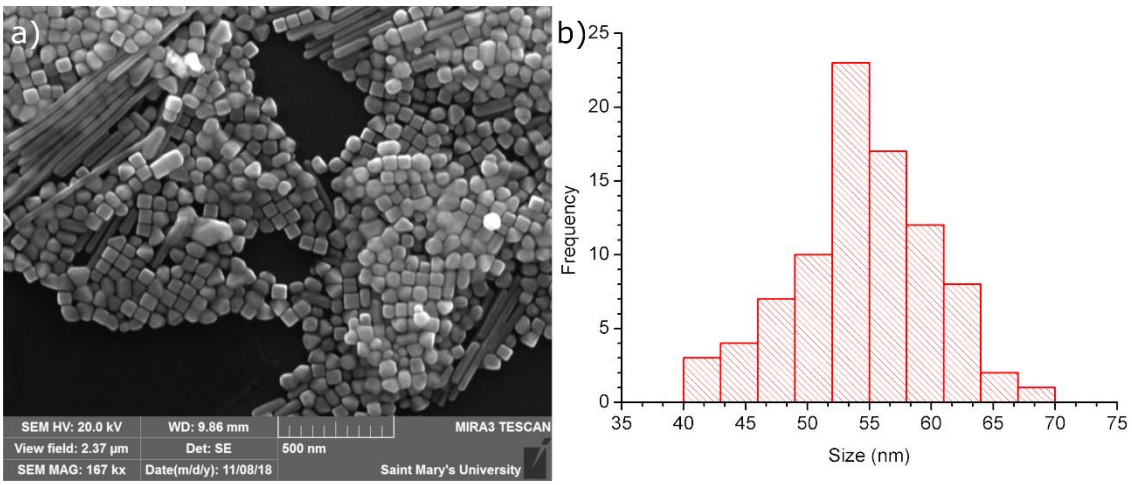

Fig. 14. a) FE-SEM micrograph of the Ag nanocubes, and b) size distribution histogram obtained by image analysis of the micrograph.

Fig. 15 shows the TEM image of the synthesized nanocubes dispersion. This micrograph confirms the presence of rounded nanocubes and additional morphologies. It can also be observed that the nanocubes tend to assembly, forming a cube array. This array also contains gaps between the edges of the cubes, these spots are ideal to produce hot-spots, and thus, a higher SERS effect. A particle size distribution obtained by image

analysis shows a distribution at a range of 25 – 65 nm, with an average size of 47 ± 6.3 nm.

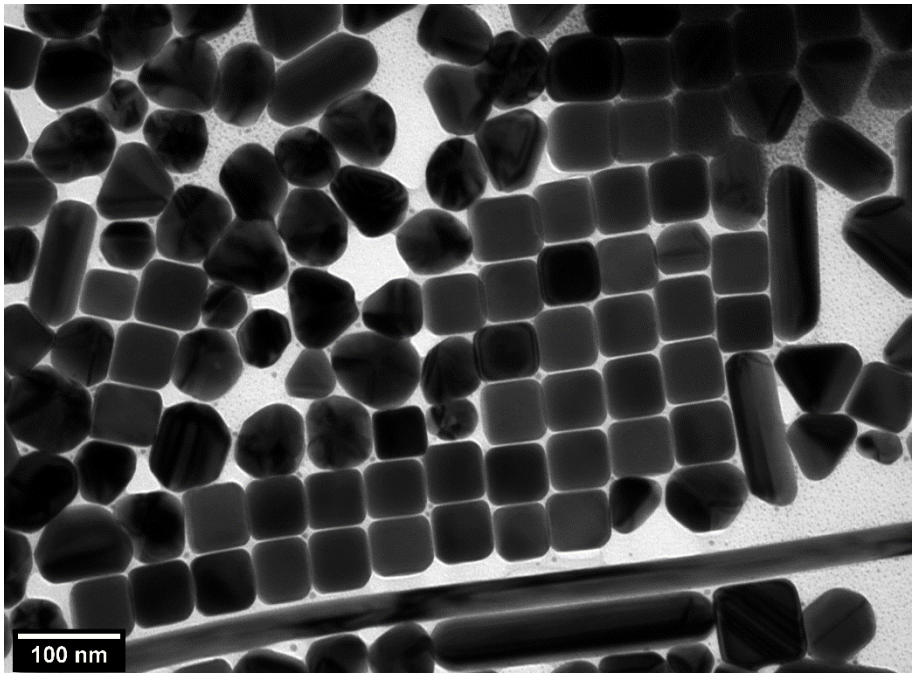

Fig. 15. TEM micrograph of the Ag nanocubes dispersion.

4.1.3 Gold nanospheres (AuNS)

The UV-Vis spectrum of the synthesized AuNS particles can be observed in Fig. 16. This analysis shows a maximum absorption band at 520 nm, which corresponds to the characteristic LSPR of Au spherical nanoparticles and their red color.

The size distribution of this dispersion was first characterized by DLS, resulting in the size histogram shown in Fig. 17. This data reflects that the nanoparticles have a hydrodyamic size between 10 and 30 nm. On the other hand, FE-SEM image were obtained to be able to see the morphology of the particles, the micrographs are shown in Fig. 18. These micrographs show spherical nanoparticles with an average diameter of 12

± 0.8 nm. Also, a size distribution histogram obtained by image analysis of 34 nanoparticles shows that the diameter of the particles is in a range between 8 and 15 nm.

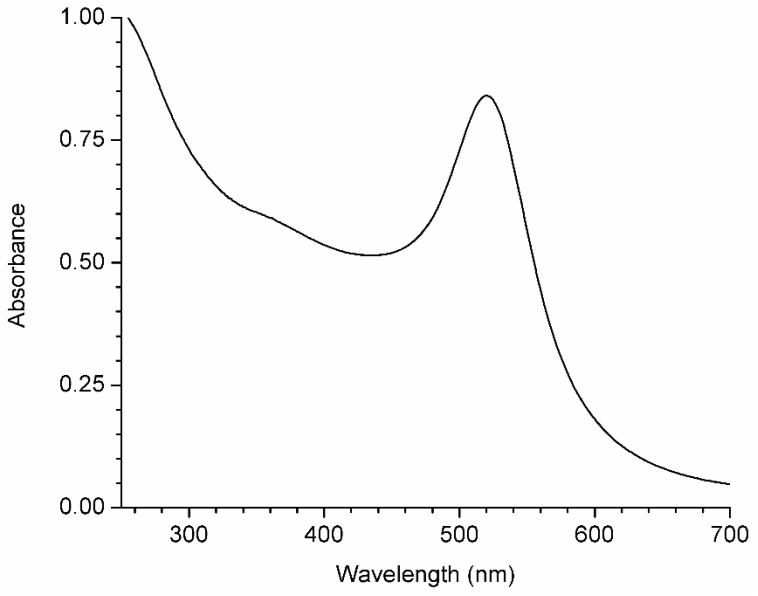

Fig. 16. UV-Vis spectrum of the Au nanospheres dispersion.

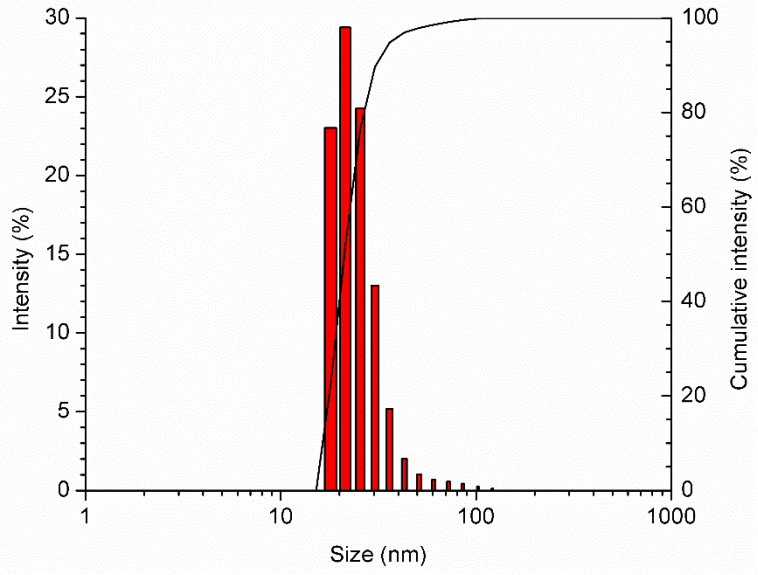

Fig. 17. DLS analysis of the Au nanospheres colloidal dispersion.

Fig. 19 shows the TEM micrograph of the AuNS dispersion. This analysis shows the obtainment of spherical nanoparticles with an average diameter of 18 ± 2.2 nm in a size distribution between 13 and 24 nm.

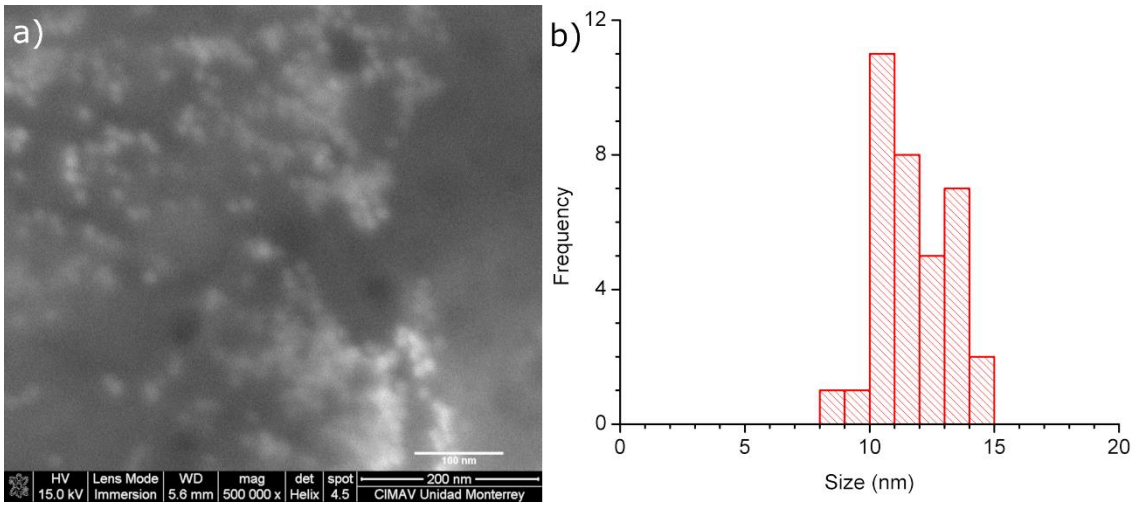

Fig. 18. a) FE-SEM micrograph of the Au nanospheres, and b) size distribution histogram obtained by image analysis of the micrograph.

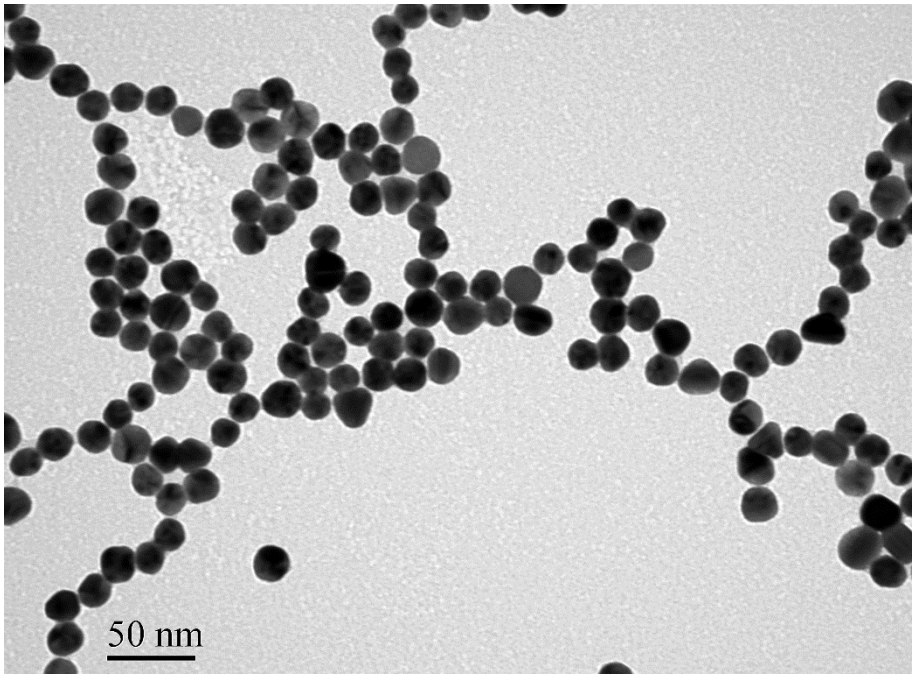

Fig. 19. TEM micrograph of the Au nanospheres dispersion.

4.1.4 Gold nanorods (AuNR)

Similarly, Fig. 20 shows the UV-Vis spectrum obtained for the AuNR. It can be observed that this spectrum contains two absorption bands, one at 520 and other at 620 nm. These two bands are the LSPR modes of the Au nanorods: the first one corresponds to the transverse mode; and the second one corresponds to the longitudinal mode. By analyzing the latter spectrum, the aspect ratio of the obtained particles can be approximated. According to the published works, the aspect ratio of Au nanorods has a direct effect on the maximum absorption wavelength of the longitudinal plasmon. Analyzing reported maximum absorption wavelength (Table 2) and comparing with the obtained AuNR, the aspect ratio of the dispersion is close to 2.0 [9,45].

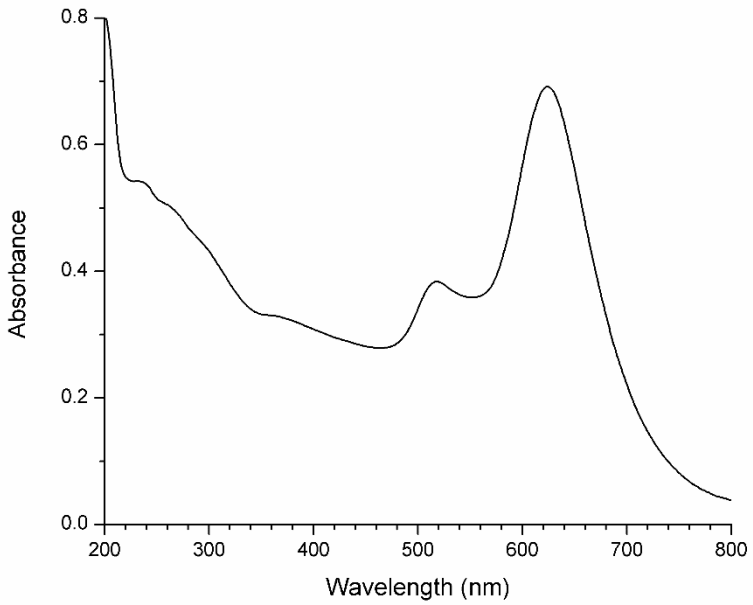

Fig. 20. UV-Vis spectrum of the Au nanorods dispersion.

On the other hand, the DLS analysis of this dispersion, presented in Fig. 21, shows a wide size distribution ranging from 40 to 200 nm. As mentioned previously, the

calculations performed during this analysis considers the particles as a hard sphere diffusing through the solvent with at a given translational diffusion coefficient, including the electrical double layer around the particle. As this technique requires the interaction of a laser with the particles, the hard sphere diameter calculated by the software will variate depending on the rod angle at the interaction moment. This will cause an apparent wide particle size distribution.

Table 2. Aspect ratio of different Au nanorod dispersions and their longitudinal plasmon mode maximum wavelength.

Aspect ratio	AuNR longitudinal LSPR (nm)
1.1	530
1.9	600
2.9	700
4.0	820

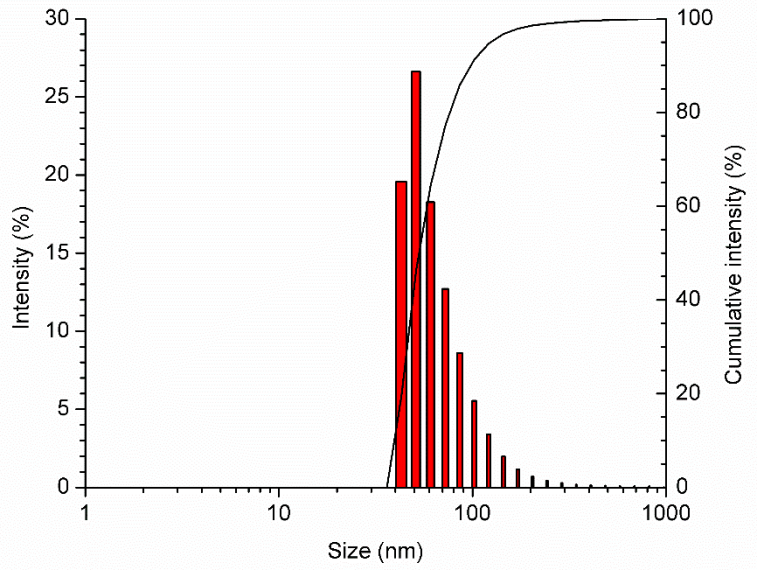

Fig. 21. DLS analysis of the Au nanorods colloidal dispersion.

Fig. 22 shows the FE-SEM micrograph of the AuNR. In this figure, we can see small rods with rounded ends and an average length and width of 50 ± 3.7 and 26 ± 2.5 nm,

respectively; also, the aspect ratio of the rods is 2.0 ± 0.2. The observed sizes and aspect ratio are consistent with the results obtained by DLS and the prediction made by analyzing the UV-Vis spectrum. The size histograms obtained by analyzing 45 particles, presented in Fig. 23, shows a narrower size distribution than the obtained by DLS, this may be caused by the presence of particle agglomerates during the DLS analysis.

In a similar way, Fig. 24 shows a TEM image of the AuNR. In this micrograph, rounded rods can be observed, having average sizes of 36 ± 5.0 and 15 ± 3.4 nm for length and width, as well as an aspect ratio of 2.5 ± 0.37. The TEM analysis shows also a length distribution between 25 and 47 nm, and a width distribution in the range of 7 to 25 nm. TEM results confirm the data obtained by the complementary techniques, allowing a complete characterization of the dispersion.

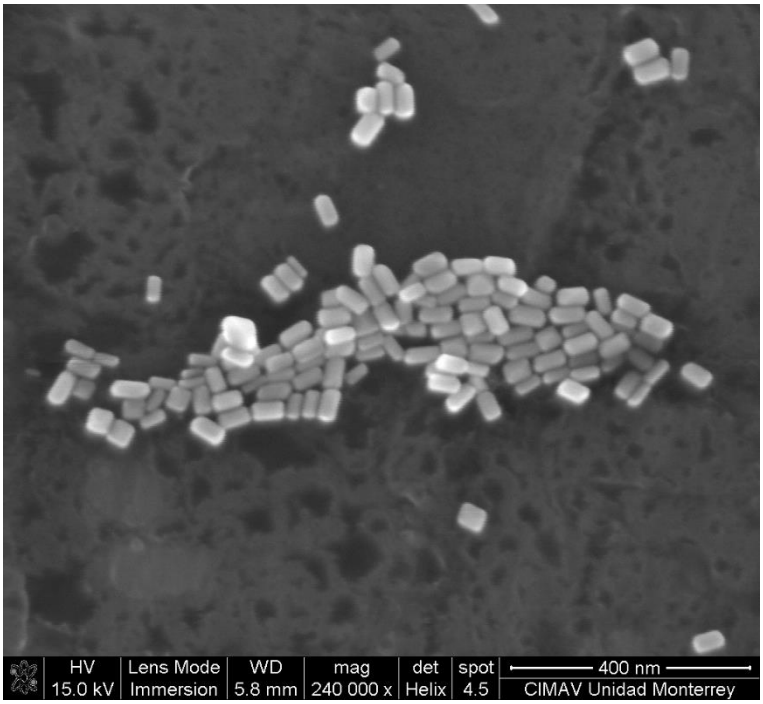

Fig. 22. FE-SEM micrograph of the Au nanorods.

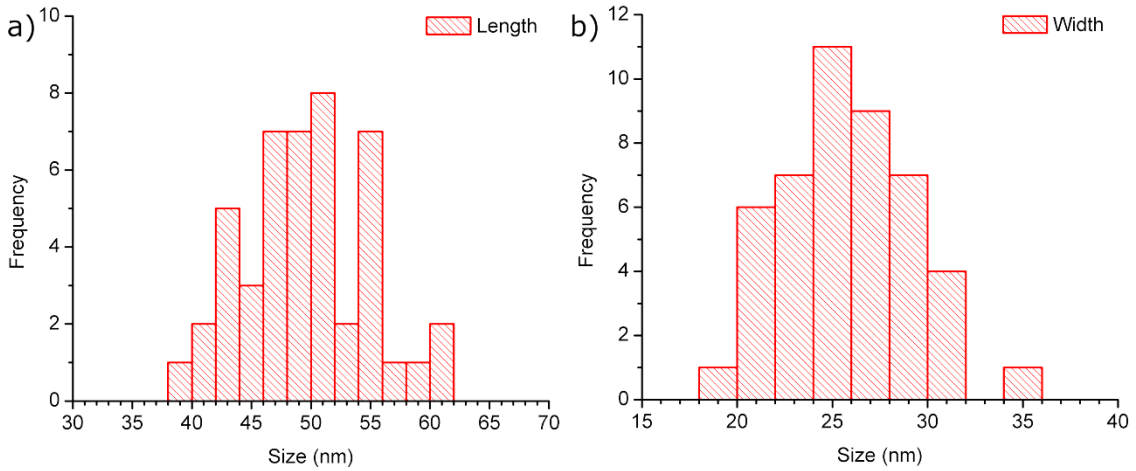

Fig. 23. Size distribution histogram of the nanorods: a) length, and b) width.

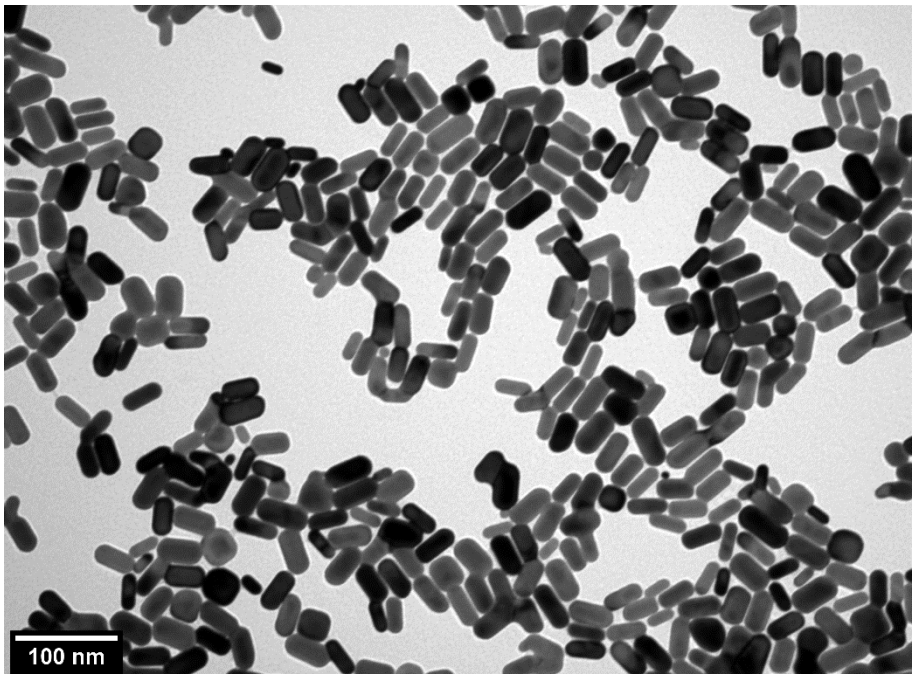

Fig. 24. TEM micrograph of the Au nanorods dispersion.

4.2 SERS substrates preparation and performance

In order to fabricate SERS substrates with the obtained nanoparticle dispersions, nanoparticle pastes were prepared. After the obtainment of each dispersion, the particles undergo a purification and concentration process by centrifugation. In this procedure, the

supernatant containing the reaction residues is eliminated, leaving a nanoparticle pellet with low solvent content; this nanoink or paste can be diluted if required and must be kept under darkness conditions to avoid its oxidation.

For the deposition of the nanoparticle pastes to fabricate SERS substrates, two different procedures were followed: a high humidity method, and a normal conditions deposition. The latter implies the direct drop-casting of 2.0 μL of the paste onto a mechanically polished Al substrate, after the drop got dry, a uniform layer of nanoparticles is obtained. This method was used for the fabrication of AgNC and AuNR SERS substrates; however, in the case of the spherical particles, the final outcome is a non-uniform particle layer. Due to the latter, variations in the procedure were investigated searching for a uniform nanoparticle layer. In the first method, a high humidity approach is used to allow the auto-assembling of the particles. In this case, the water vapor pressure acts directly on the particle drop, flattening the drop itself and pushing the particles downwards, making the spheres assembly and thus, producing a uniform substrate. This procedure, although is slower, works perfectly for spherical nanoparticles. In a parallel way, these pastes can be used to fabricate EC-SERS electrodes, as mentioned in the Appendix section.

After the obtainment of the nanoparticle layer, the next step on the SERS substrate fabrication is the addition of a chitosan layer. The effect of the chitosan solution concentration on the Raman band intensity enhancement was quickly studied by comparing the results of substrates without any chitosan and substrates with chitosan at a concentration of 0.125 and 0.250% w/v in 1% v/v CH_3COOH. All Raman spectra were recorded using 1 mM *p*-ATP as probe molecule.

Fig. 25 shows the Raman spectra obtained using the SERS substrates with different chitosan concentrations. In this figure, it can be observed that the addition of a chitosan layer has different impact on the Raman intensities depending on the dispersion used on the substrate.

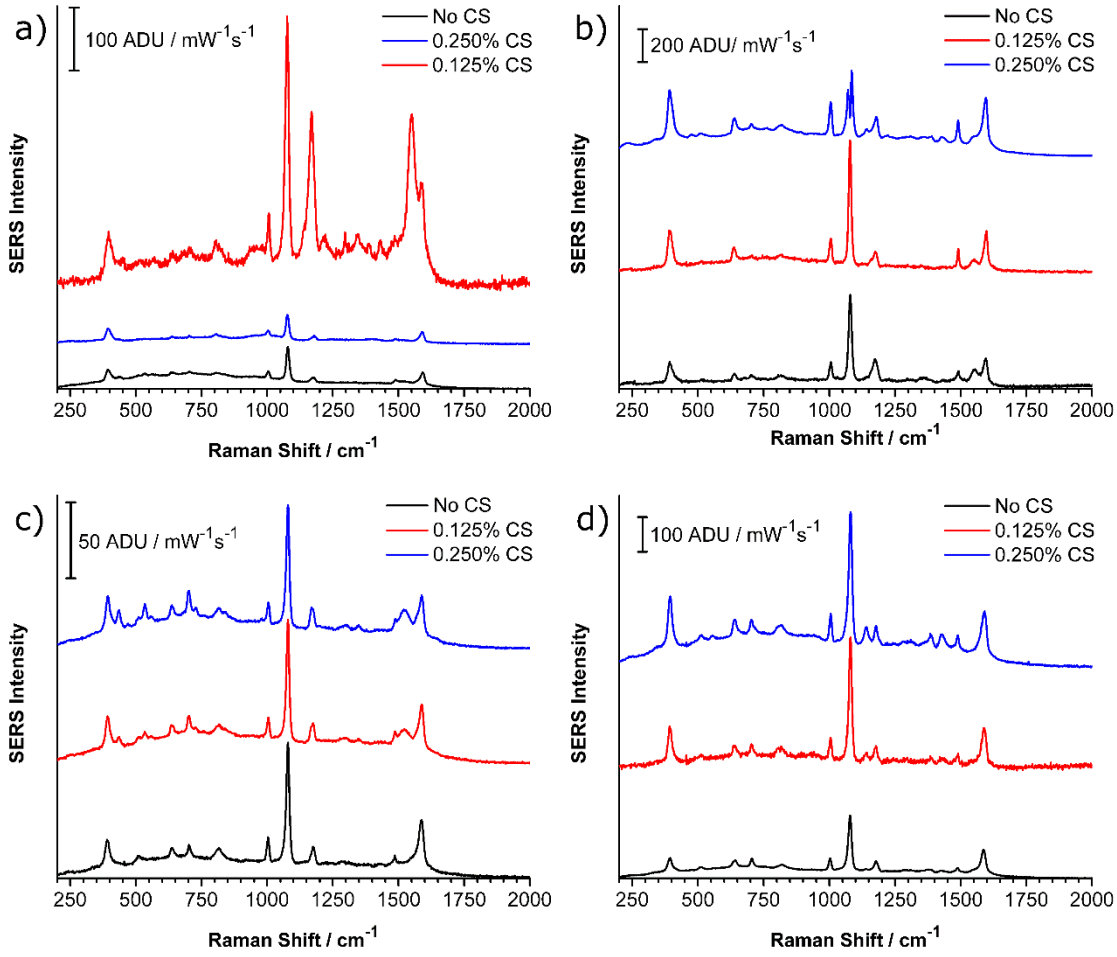

Fig. 25. Raman spectra of the SERS substrates with different chitosan concentrations: a) AgNS, b) AgNC, c) AuNS, and d) AuNR.

In the case of the AgNS substrates, a 0.25% chitosan layer is thick enough to reduce the interactions between the nanoparticles and the probe molecules, leading to lower Raman intensities. However, a chitosan layer produced using a 0.125% solution results in

a Raman spectrum with higher intensities than those obtained by the SERS substrates without any chitosan, in which there is no additional coating between the nanoparticles and the analyte molecules. Similarly, the substrates based on AgNC show reduced Raman intensities (compared with the normal SERS substrates) when a 0.25% chitosan coating is used, and higher intensities when the chitosan used is at a 0.125% concentration.

On the other hand, a chitosan coating do not affect the bands intensities when the substrate is based on AuNS, as it can be observed in Fig. 25(c). The latter is similar to the results obtained using AuNR as the active coating; however, in this case, the intensities reached are higher than the ones in the SERS substrate without chitosan.

The enhancement in the Raman band intensities may be produced by different factors such as an increase in the local electromagnetic field caused by the anisotropic nanostructures, the roughness of the final substrate, or higher inelastic scattering rates produced by the adsorption of the analyte molecules onto the chitosan coating.

The latter effect can be modified by changing the chitosan coating thickness. A thicker layer establishes a larger distance between the probe molecules and the nanostructure plasmons, leading to reduction in the SERS effect. In contrast, with a thinner chitosan coating, the molecules are closer to the plasmonic array and the enhanced local electromagnetic field has a higher effect on the molecule polarizability; and thus, higher Raman intensities can be reached.

This behavior can be observed in the results obtained in Fig. 25, in which the use of a concentrated chitosan solution leads to intensities as high as or lower than those obtained by a normal SERS substrate due to the distance between the particles and the molecules.

However, using a diluted solution, the obtained polymer coating is thinner and thus allows a higher interaction between the array and the adsorbed species, leading to higher Raman intensities. Due to these results, 0.125% was selected as the suitable chitosan concentration for all following experiments.

After choosing a chitosan concentration to work with, the effect of the polymer molecular weight on the SERS intensities enhancement was analyzed. For this, chitosan with three different molecular weights were used: 50 – 190, 190 – 310, and 310 – 375 kDa, from now on referred to as low, medium and high molecular weights, respectively. The weights were determined by Sigma Aldrich by viscosity measurements.

Fig. 26 shows micrographs of the three different chitosan solutions deposited onto Al substrates. In order to image any chitosan-containing substrate, the sample was Au-coated. It was found that the electron beam from the microscope is energetic enough to break the chitosan coating by breaking the matrix itself; this behavior also occurs when the deposited Au coating is thin, impeding the recording of a representative image. In these micrographs, the morphology of the chitosan can be observed as a uniform coating with cracks. It is unclear if the cracks are formed during the drop coating process or if they were created during the FE-SEM imaging. On the other hand, it can be concluded that the general morphology of the chitosan coating with different molecular weights is the same.

With the SEM analysis and knowing the effect of the chitosan thickness on the SERS enhancement, some predictions can be made. According to the obtained results, and even though the morphology of the chitosan layers is the same, using the high molecular weight chitosan may produce a thicker coating, which will produce a decrease in the SERS

enhancement. Following the same idea, the substrates fabricated with the low molecular weight chitosan would show the highest Raman intensities due to the shorter distance between the nanoparticles and the probing molecules.

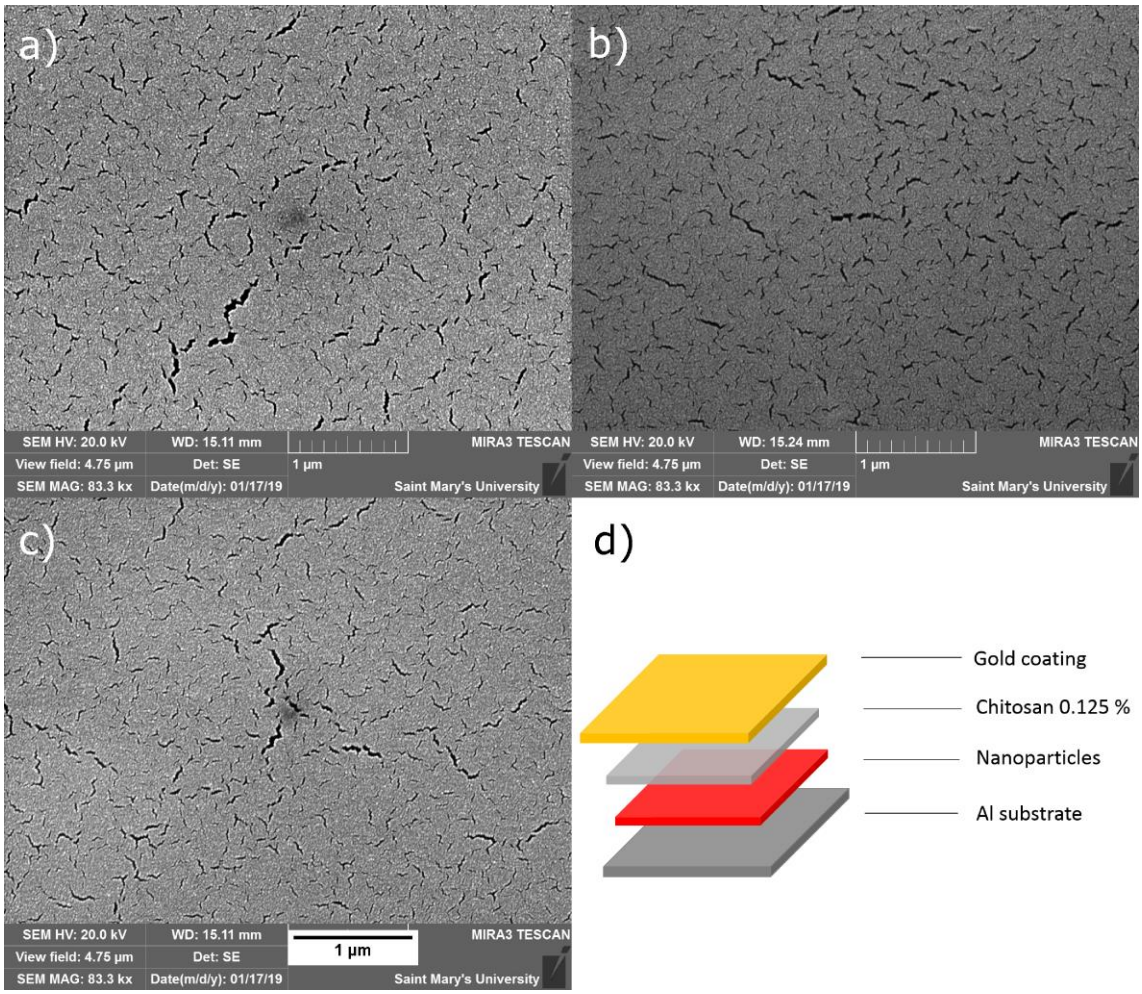

Fig. 26. FE-SEM images of chitosan at 0.125% w/v with different molecular weights.

Similarly, Fig. 27 shows the FE-SEM and Raman analysis of the substrates fabricated with AgNS and chitosan with different molecular weights at 0.125% w/v in 1% v/v CH_3COOH. These micrographs show the same chitosan matrix with cracks that was observed previously in the chitosan samples. Nevertheless, brighter zones can be observed in the AgNS substrates, which can be produced by the presence of areas with packed

nanoparticle agglomerates. Ideally, the SERS enhancement is higher when the probe molecules are adsorbed close to these brighter zones, due to the influence of the plasmons produced by the nanospheres agglomerate. On the other hand, darker spots can also be observed in the micrographs; these spots irregularities in the chitosan matrix with the form of small bumps made of chitosan, as the chitosan is an organic compound, these irregularities are recorded as darker spots.

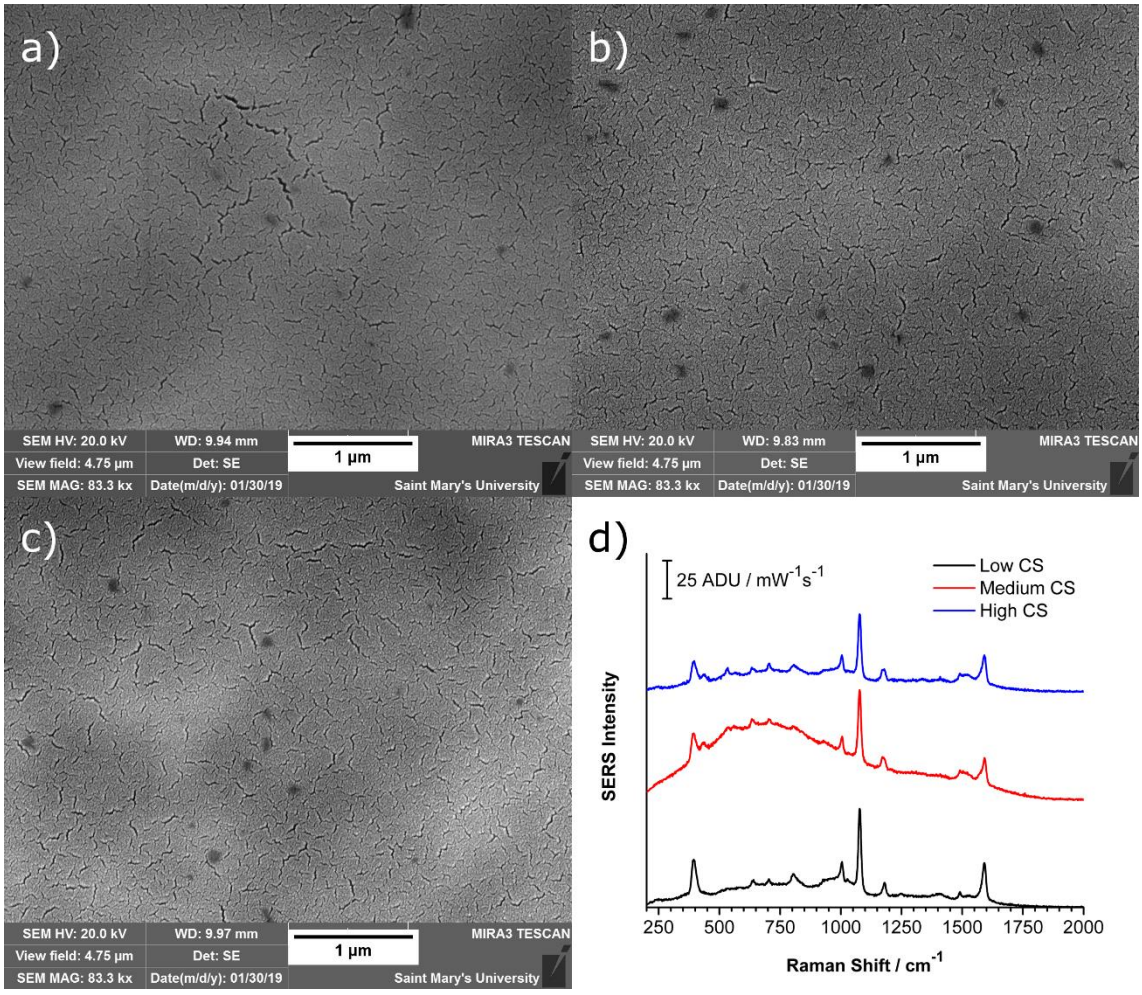

Fig. 27. FE-SEM images of the AgNS substrates with chitosan at 0.125% w/v with a) low, b) medium, and c) high molecular weight, and d) their Raman spectra using 1 mM *p*-ATP as analyte.

Fig. 27(d) shows the Raman spectra obtained by the three substrates using 1 mM *p*-ATP as the analyte. The comparison between the spectra shows that the use of chitosan with different molecular weights do not affect the SERS enhancement when Ag nanospheres are used as active plasmonic layer. These results are not consistent with the predictions based on the chitosan molecular weight and the distance between the adsorbed molecules and the nanoparticles array.

In the case of the substrates based on a AgNC layer, the Fig. 28 shows the FE-SEM micrographs of the substrates with different chitosan molecular weights, as well as their Raman spectra with *p*-ATP as probe molecule. The morphology of these substrates is completely different than the AgNS substrates. The nanostructures are thick enough to be observed through the thin chitosan coating; however, due to the polymeric matrix, the particles show cube-like, rod and spherical shapes, some cracks in the chitosan can also be found in the micrographs. The roughness of the AgNC substrates may be the factor that leads to SERS enhancements as high as the obtained in this work, when comparing with the substrates fabricated with spherical particles.

On the other hand, the Raman spectra obtained using the AgNC-based substrates show similar band intensities. These results are similar to those obtained by using AgNS as the active SERS layer, thus concluding that the molecular weight of the chitosan used to coat the SERS substrates do not affect the plasmonic enhancement when the nanostructures used are composed of Ag.

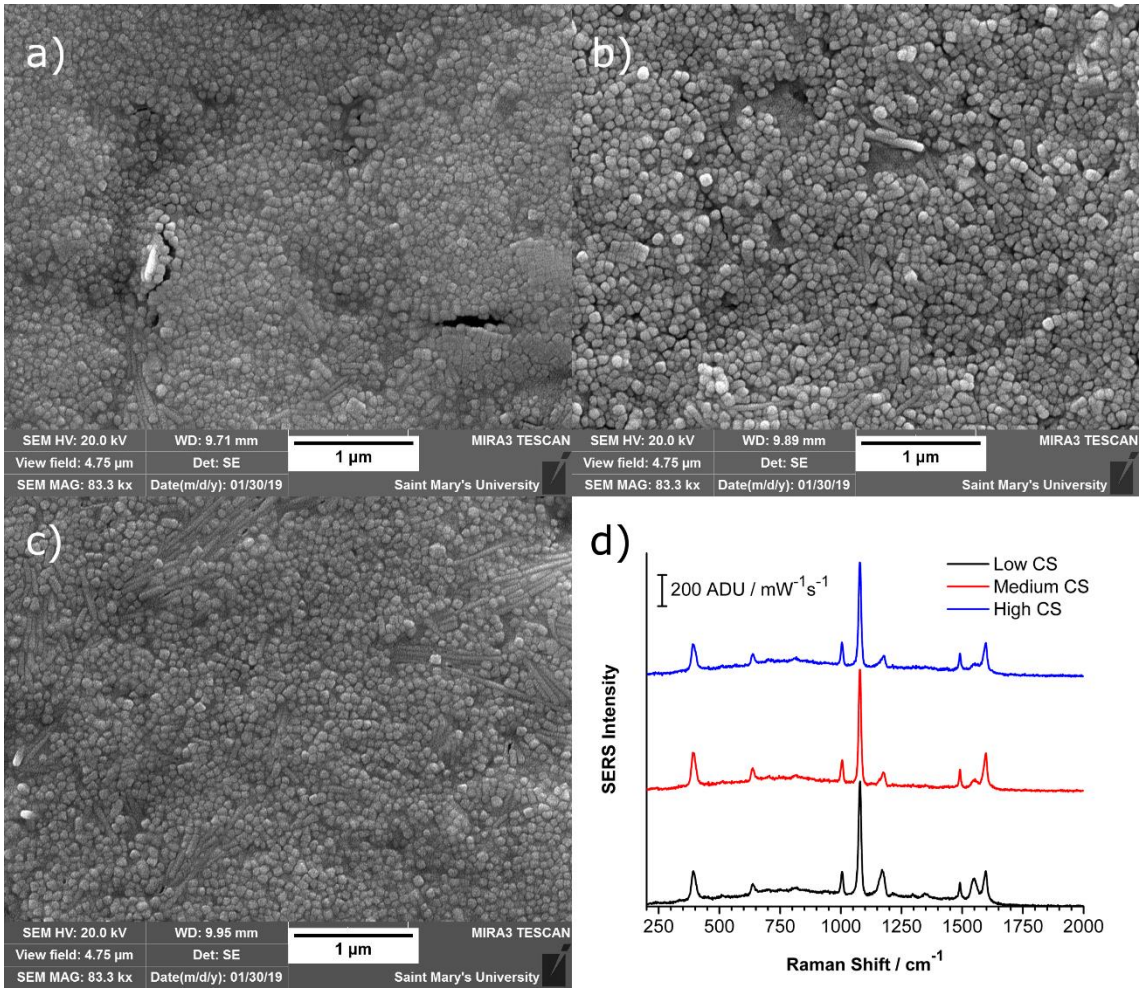

Fig. 28. FE-SEM images of the AgNC substrates with chitosan at 0.125% w/v with a) low, b) medium, and c) high molecular weight, and d) their Raman spectra using 1 mM *p*-ATP as analyte.

Fig. 29 presents the FE-SEM micrographs of the AuNS-based substrates and their Raman spectra. In this case, the micrographs show a high number of agglomerated particles as the substrate surface; these particles are probably the Au coating required in order to image the substrate, avoiding a proper visualization of the chitosan surface. However, in the micrograph shown in Fig. 29(c), the surface of the AuNS-CS_{high} substrate can be appreciated with more detail. The surface of this substrate is similar to the chitosan coating by itself: a uniform polymeric matrix with cracks; nevertheless, brighter zones are

observed in this micrograph, similarly to those observed in the AgNS substrates. These zones are areas with a high number of Au nanospheres together, and as they are under the chitosan coating, the image appears to be blurry; however, the substrate surface is focus, and thus, the cracks in the polymer can be observed.

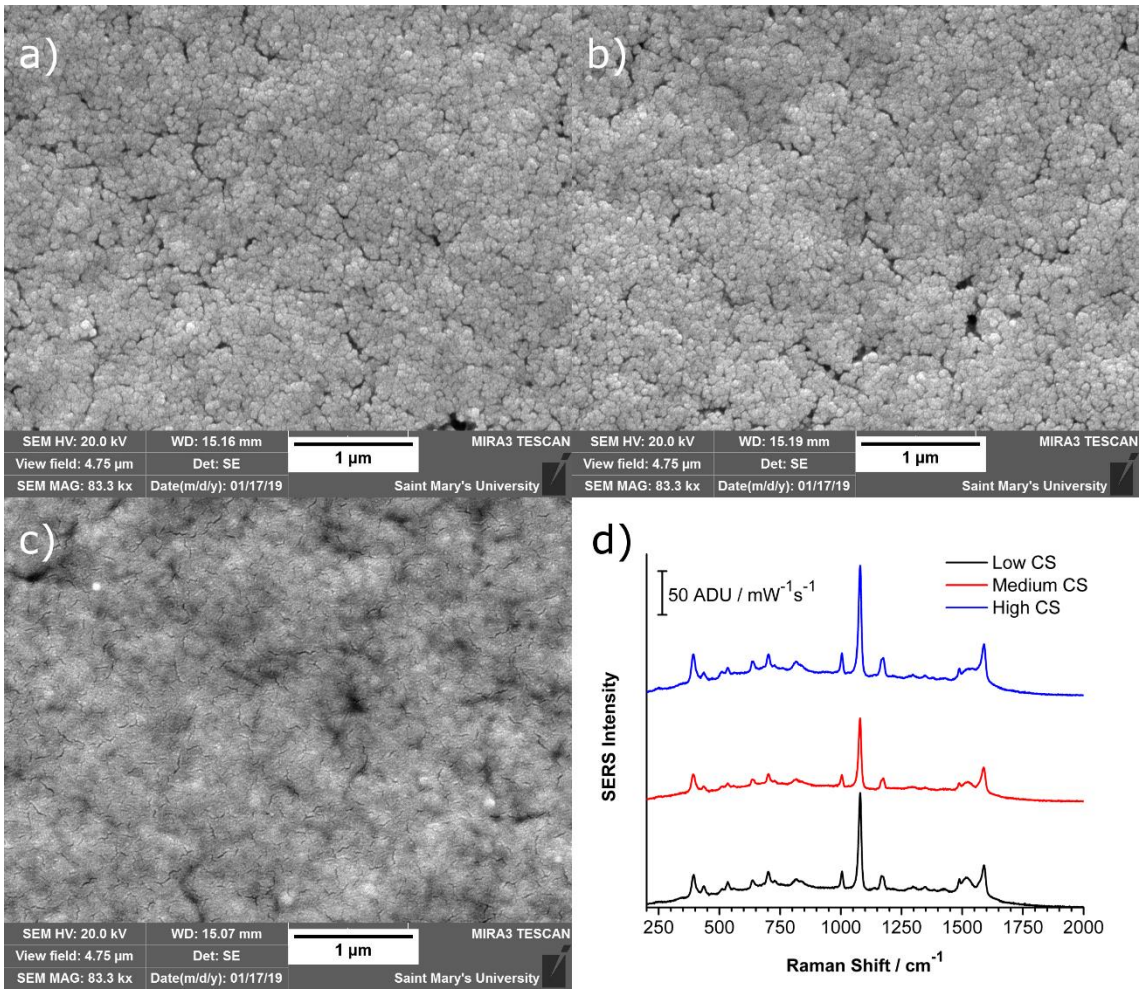

Fig. 29. FE-SEM images of the AuNS substrates with chitosan at 0.125% w/v with a) low, b) medium, and c) high molecular weight, and d) their Raman spectra using 1 mM *p*-ATP as analyte.

The Raman spectra shown in Fig. 29(d) represent the SERS performance of each substrate fabricated using AuNS as the plasmonic layer and chitosan with different molecular weight. In this case, the Raman intensities obtained are similar when low and

high chitosan are used. Nevertheless, the substrate fabricated with chitosan at a medium molecular weight shows bands with lower intensities than those reached with low and high chitosan. Also, the spectrum recorded using the high chitosan shows slightly higher intensities than the bands in the low chitosan substrate. On the other hand, these substrates show better results than the substrates based on AgNS, but the cubic nanostructures reached the highest intensities until this point of the project.

In a similar way, Fig. 30 shows the FE-SEM and Raman analysis of the SERS substrates based on AuNR and chitosan. The surface of these substrates, observed in the micrographs, is similar to the surface of the AuNS-based substrates: a uniform polymeric matrix with cracks along the chitosan; brighter zones produced by the presence of agglomerated Au nanorods from the plasmonic layer can also be observed. In the case of chitosan with medium and high molecular weight, the nanoparticle distribution along the Al produced thicker zones, changing the roughness of the final substrate. As reviewed before, the roughness of a SERS substrate also affects the Raman intensities enhancement.

The Raman spectra presented in Fig. 30(d) allows a comparison between the three AuNR-based substrates. It can be observed that the intensities reached do not change drastically depending on the molecular weight of the chitosan; however, the substrate fabricated with the medium chitosan shows the highest bands intensities of the three. On the other hand, these substrates show better results than those obtained using spherical nanoparticles as SERS-active layers, but lower intensities than those reached by using a coating of Ag nanocubes.

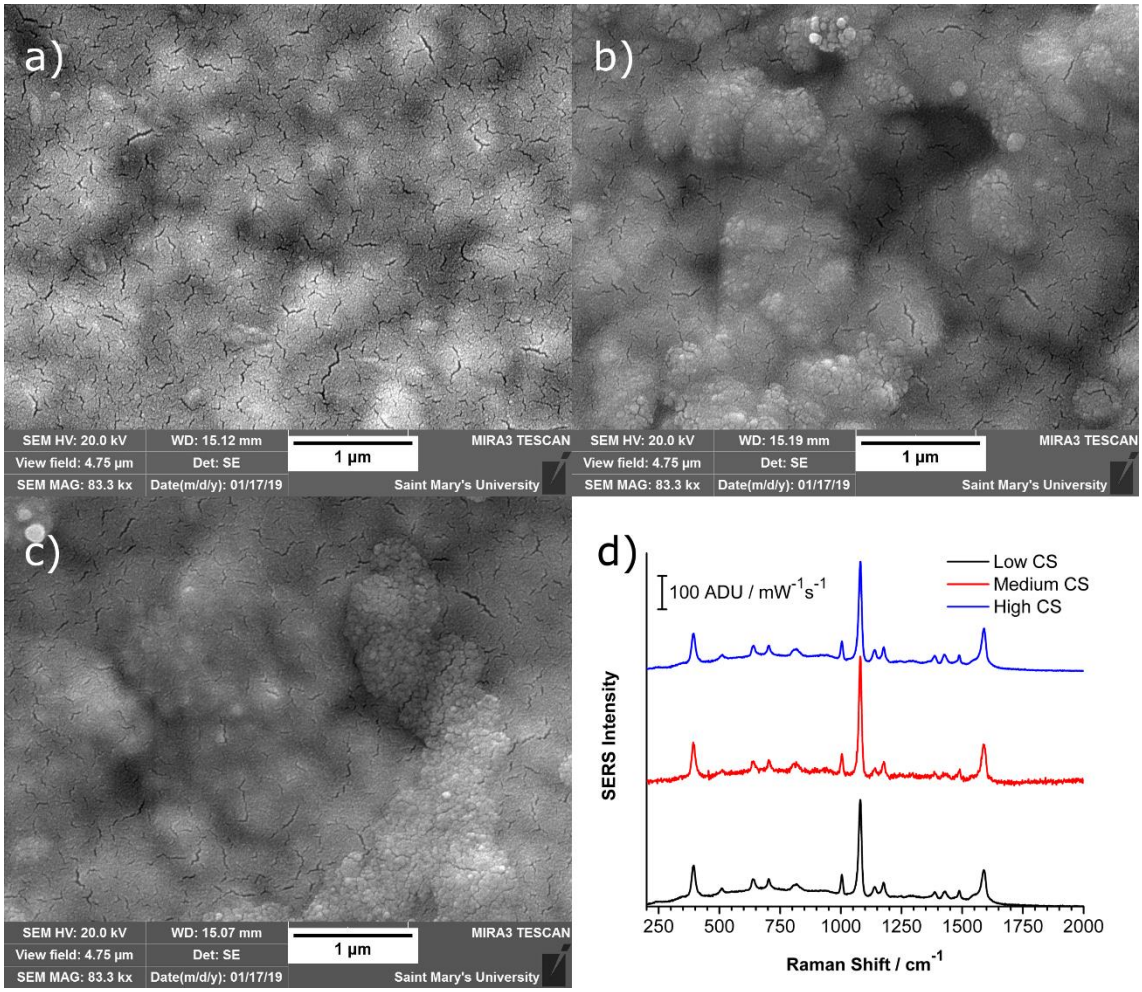

Fig. 30. FE-SEM images of the AuNR substrates with chitosan at 0.125% w/v with a) low, b) medium, and c) high molecular weight, and d) their Raman spectra using 1 mM *p*-ATP as analyte.

Based on the results obtained during this section of the project, the best substrate of each nanoparticle morphology was selected and used for the analysis of the limit of detection. For the AgNS, AgNC, and AuNR, the substrate fabricated with chitosan with a medium molecular weight showed the highest Raman intensities; and thus, these substrates were selected and used for the next section. In the case of AuNS, the substrate obtained using a high molecular weight chitosan coating reached the best intensity enhancement, and so it was used for the limit of detection analysis.

4.3 Limit of detection analysis

In order to analyze the lowest concentration that can be detected by each substrate, *p*-ATP solutions were prepared at a concentration range of 10^{-3} to 10^{-9} M, 2 μL of each solution was deposited onto the substrates and let dry before performing the spectroscopic analysis. The substrates used fabricated using chitosan at a concentration of 0.125% w/v in 1% v/v CH_3COOH; in the case of the chitosan molecular weight, the substrates based on AgNS, AgNC and AuNR use the polymer at a medium molecular weight, and the AuNS substrate uses high molecular weight chitosan.

Fig. 31 shows the limit of detection reached with each nanostructured substrate presented as the *p*-ATP Raman spectra of the detectable solutions at each particle case. For the substrates based on Ag nanospheres and medium chitosan the limit of detection reaches 10^{-4} M; as observed in the spectra, the outcome of analyzing a 10^{-5} M solution is a spectrum with only the substrate's background signals, which can still be observed when analyzing a 10^{-4} M solution, nevertheless, the most intense *p*-ATP vibrational bands can be observed.

On the other hand, the substrates fabricated using a AgNC-active coating and medium molecular weight chitosan can detect solutions as diluted as 10^{-9} M. Although Fig. 31(b) shows the complete limit of detection analysis of this kind of substrates, Fig. 32 presents the spectra of the solutions within the 10^{-9} and 10^{-5} M concentration range in more detail. In this figure, it can be observed that the 10^{-9} M solutions produces a spectrum where the Ag-Cl stretching band (at 242 cm^{-1}) has a higher intensity than the *p*-ATP bands [80];

however, as the solution gets more concentrated, the intensity of the analyte bands increase and the Ag-Cl band intensity decreases. An important point of this study is the drastic intensities enhancement that occurs between the 10^{-6} and 10^{-5} M solutions, which may suggest the existence of a threshold concentration required in order to produce a significant enhancement.

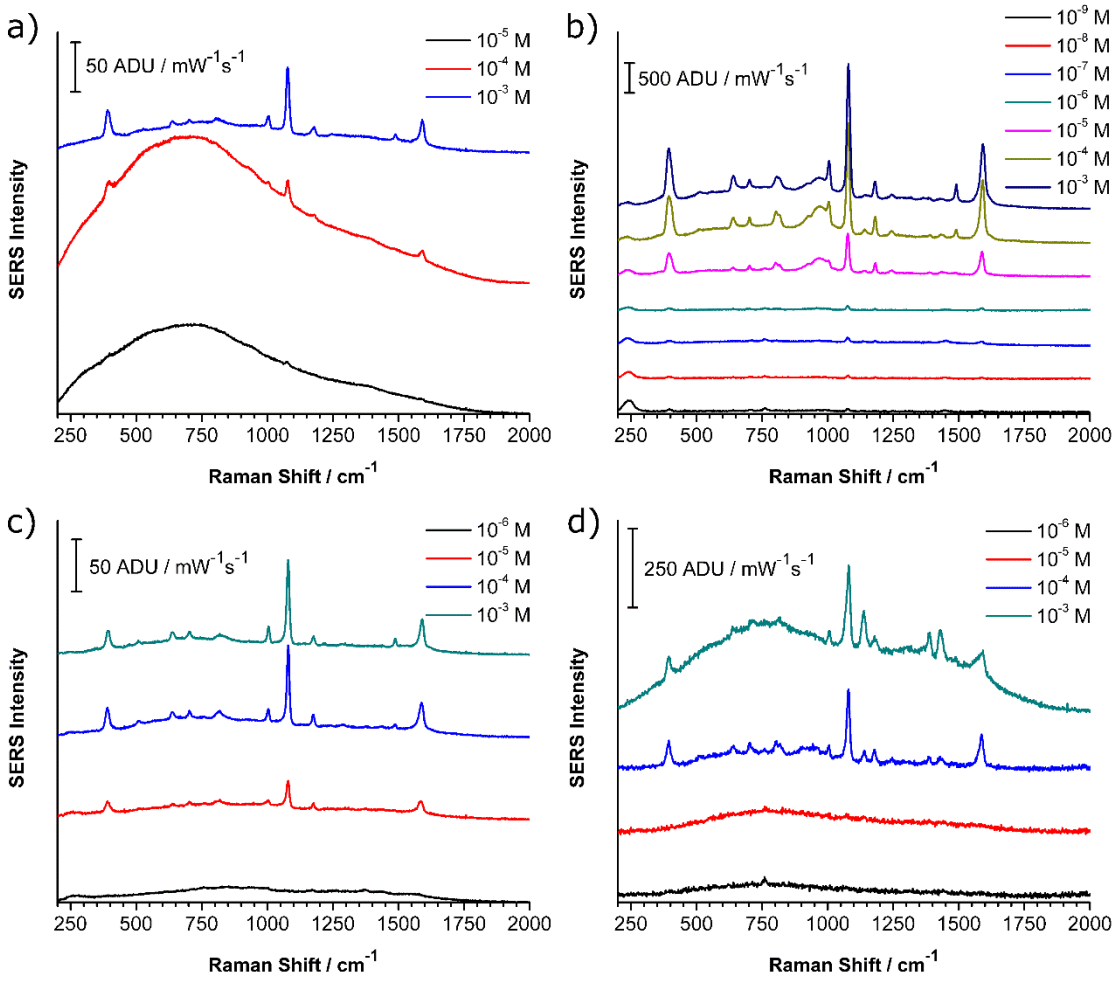

Fig. 31. Limit of detection study of a) AgNS-CS_{med}, b) AgNC-CS_{med}, c) AuNS-CS_{high}, and d) AuNR-CS_{med} substrates.

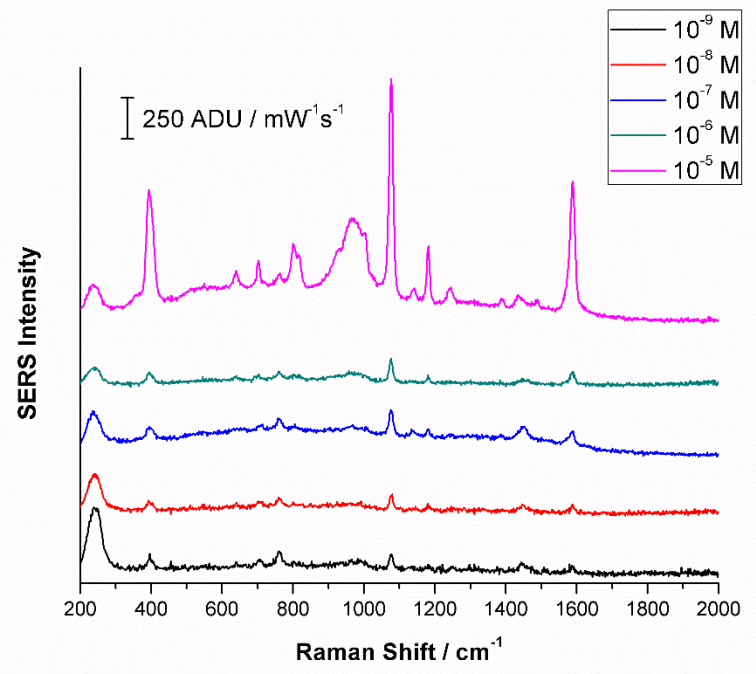

Fig. 32. Limit of detection study of the AgNC-CS_{med} substrates at the concentration range of 10^{-9} to 10^{-5} M.

In Fig. 31(c) the detection limit study of the AuNS-CS_{high} substrates is presented. In this case, the lowest detectable *p*-ATP concentration is 10^{-5} M, and no background bands are presented in any of the recorded spectra. This limit is better than the obtained by the AgNS-based substrates, but the AgNC substrates showed a lower limit.

In contrast, the results obtained by the AuNR-CS_{med} substrates are presented in Fig. 31(d). In this case, the spectra show a lower signal/noise ratio, however, the *p*-ATP signals can be easily observed. The lowest analyte concentration detected by this kind of substrates is 10^{-4} M, similarly to the AgNS-based substrates.

The results obtained in this section of the project make possible to conclude that the hypothesis is approved for the AgNC-based substrates, while it is rejected for the AgNS, AuNS and AuNR substrates. Based on the obtained results, the AgNC-CS_{med} substrates

can be used to analyze probe molecules at concentrations lower than 10^{-3} M, this capacity can be further enhanced if the analyte contains thiol groups or moieties with free electron pairs that can interact directly with the Ag particles. On the other hand, using Au nanoparticles as SERS-active coating is useful when a higher stability and biocompatibility is required; in this case, AuNS-CS_{high} substrates may reach better results.

CHAPTER 5

CONCLUSIONS

Based in the results obtained during this project, it is possible to conclude:

1. The AgNS, AgNC, AuNS, and AuNR dispersions obtained during this project, showed high purity, and suitable shape and particle size distribution for their use as SERS substrate; this affirmation is based on their UV-Vis spectra, DLS analysis, and electron microscopies.

2. Pastes based on each nanostructure dispersion were obtained by centrifugation and successfully used to fabricate uniform SERS substrates by a drop-casting method at normal (AgNC and AuNR) and high humidity conditions (AgNS and AuNS).

3. The effect of the chitosan solution concentration on the SERS enhancement was studied by analyzing the performance of bare and chitosan-covered SERS substrates, using 1 mM *p*-ATP as Raman probe molecule. The Raman spectra showed that using a 0.125% w/v chitosan solution leads to a higher Raman intensities enhancement, and thus, this concentration was used in the further experiments.

4. A study about the effect of the chitosan's molecular weight on the Raman intensity enhancements was also performed. Substrates were fabricated using the nanostructures and chitosan solutions. This parameter do not strongly impact the SERS maximum enhancement; however, the substrates containing a CS_{med} coating reached the highest intensities for AgNS, AgNC, and AuNR, whereas the CS_{high} showed the best enhancement for the AuNS products.

5. A study of the limit of detection was performed for each kind of substrate, using *p*-ATP at a concentration range between 10^{-3} and 10^{-9} M. The results showed the following limits of detection: 10^{-4} M for AgNS, 10^{-9} M for AgNC, 10^{-5} M for AuNS, and 10^{-4} M for AuNR, rejecting the stated hypothesis for the AgNS, AuNS, and AuNR systems, and accepting it for the AgNC substrates.

REFERENCES

1. Cobley, C.M.; Skrabalak, S.E.; Campbell, D.J.; Xia, Y. Shape-controlled synthesis of silver nanoparticles for plasmonic and sensing applications. Plasmonics, 2009, 4 (2), pp. 171-179.

2. Zheng, X.; Peng, Y.; Cui, X.; Zheng, W. Modulation of the shape and localized surface plasmon resonance of silver nanoparticles via halide ion etching and photochemical regrowth. Materials Letters, 2016, 173, pp. 88-90.

3. Liu, Y.; Han, X.; He, L.; Yin, Y. Thermoresponsive assembly of charged gold nanoparticles and their reversible tuning of plasmon coupling. Angewandte Chemie International Edition, 2012, 51 (26), pp. 6373-6377.

4. Wang, Y.; Yang, F.; Yang, X. Colorimetric detection of mercury(II) ion using unmodified silver nanoparticles and mercury-specific oligonucleotides. ACS Applied Materials & Interfaces, 2010, 2 (2), pp. 339-342.

5. Giovannozzi, A.M.; Rolle, F.; Sega, M.; Abete, M.C.; Marchis D.; Rossi, A.M. Rapid and sensitive detection of melamine in milk with gold nanoparticles by surface enhanced Raman scattering. Food Chemistry, 2014, 159, pp. 250-256.

6. Suvith, V.S.; Philip, D. Catalytic degradation of methylene blue using biosynthesized gold and silver nanoparticles. Spectrochimica Acta Part A: Molecular and Biomolecular Spectroscopy, 2014, 118, pp. 526-532.

7. Saxena, A.; Tripathi, R.M.; Zafar, F.; Singh, P. Green synthesis of silver nanoparticles using aqueous solution of Ficus benghalensis leaf extract and characterization of their antibacterial activity. Materials Letters, 2012, 67 (1), pp. 91-94.

8. Cao, J.; Sun, T.; Grattan, K.T.V. Gold nanorod-based localized surface plasmon resonance biosensors: A review. Sensors and Actuators B: Chemical, 2014, 195, pp. 332-351.

9. Qiu, Y.; Liu, Y.; Wang, L.; Xu, L.; Bai, R.; Ji, Y.; Wu, X.; Zhao, Y.; Li, Y.; Chen, C. Surface chemistry and aspect ratio mediated cellular uptake of Au nanorods. Biomaterials, 2010, 31 (30), pp. 7606-7619.

10. Hung, I.; Lee, S.Y.; McGovern, O.; Rabin, O.; Mayergoyz, I. Calculation and measurement of radiation corrections for plasmon resonances in nanoparticles. Physical Review B, 2013, 88, pp. 1-9.

11. Liu, P.; Yang, X.; Sun, S.; Wang, Q.; Wang, K.; Huang, J.; Liu, J.; He, L. Enzyme-free colorimetric detection of DNA by using gold nanoparticles and hybridization chain reaction amplification. Analytical Chemistry, 2013, 85 (16), pp. 7689-7695.

12. Stewart, A.; Murray, S.; Bell, S.E.J. Simple preparation of positively charged silver nanoparticles for detection of anions by surface-enhanced Raman spectroscopy. Analyst, 2015, 140 (9), pp. 2988-2994.

13. Tang, Y.; Yang, Q.; Wu, T.; Liu, L.; Ding, Y.; Yu, B. Fluorescence enhancement of cadmium selenide quantum dots assembled on silver nanoparticles and its application to glucose detection. Langmuir, 2014, 30 (22), pp. 6324-6330.

14. Stiles, P.L.; Dieringer, J.A.; Shah, N.C.; Van Duyne, R.P. Surface-enhanced Raman spectroscopy. Annual Review of Analytical Chemistry, 2008, 1 (1), pp. 601-626.

15. Cantarero, A. Raman scattering applied to materials science. Procedia Materials Science, 2015, 9, pp. 113-122.

16. López-López, M.; García-Ruiz, C. Infrared and Raman spectroscopy techniques applied to identification of explosives. TrAC Trands in Analytical Chemistry, 2014, 54, pp. 36-44.

17. Tuma, R. Raman spectroscopy of proteins: from peptides to large assemblies. Journal of Raman Spectroscopy, 2005, 36 (4), pp. 307-319.

18. Mazzella, W.D.; Buzzini, P. Raman spectroscopy of blue gel pen inks. Forensic Science International, 2005, 152 (2-3), pp. 241-247.

19. Frías, M.; Martínez-Ramírez, S. Use of micro-Raman spectroscopy to study reaction kinetics in blended white cement pastes containing metakaolin. Journal of Raman Spectroscopy, 2009, 40 (12), pp. 2063-2068.

20. Fleischmann, M.; Hendra, P.J.; McQuillan, A.J. Raman spectra of pyridine adsorbed at a silver electrode. Chemical Physics Letters, 1974, 26 (2), pp. 163-166.

21. Jeanmaire, D.L.; Van Duyne, R.P. Surface raman spectroelectrochemistry: Part I. Heterocyclic, aromatic, and aliphatic amines adsorbed on the anodized silver electrode. Journal of Electroanalytical Chemistry and Interfacial Electrochemistry, 1977, 84 (1), pp. 1-20.

22. King, F.W.; Van Duyne, R.P.; Schatz, G.C. Theory of Raman scattering by molecules adsorbed on electrode surfaces. The Journal of Chemical Physics, 1978, 69 (10), pp. 4472-4481.

23. Moskovits, M. Surface roughness and the enhancedintensity of Raman scattering by moleculesadsorbed on metals. The Journal of Chemical Physics, 1978, 69 (9), pp. 4159-4161.

24. Valley, N.; Greeneltch, N.; Van Duyne, R.P.; Schatz, G.C. A look at the origin and magnitude of the chemical contribution to the enhancement mechanism of surface-enhanced Raman spectroscopy (SERS): theory and experiment. The Journal of Physical Chemistry Letters, 2013, 4 (16), pp. 2599-2604.

25. Lombardi, J.R.; Birke, R.L.; Lu, T.; Xu, J. Charge-transfer theory of surface enhanced Raman spectroscopy: Herzberg–Teller contributions. The Journal of Chemical Physics, 1986, 84 (8), pp. 4174-4180.

26. Sharma, B.; Frontiera, R.R.; Henry, A.-I.; Ringe, E.; Van Duyne, R.P. SERS: Materials, applications, and the future. Materials Today, 2012, 15 (1-2), pp. 16-25.

27. Boujday, S.; de la Chapelle, M.L.; Srajer, J.; Knoll, W. Enhanced Vibrational Spectroscopies as Tools for Small Molecule Biosensing. Sensors, 2015, 15, pp. 21239-21264.

28. Stiles, P.L.; Dieringer, J.A.; Shah, N.C.; Van Duyne, R.P. Surface-Enhanced Raman Spectroscopy, 2008, 1, pp. 601-626.

29. Grasseschi, D.; Toma, H.E. The SERS effect in coordination chemistry. Coordination Chemistry Reviews, 2017, 333, pp. 108-131.

30. Esenturk, E.N.; Walker, A.R.H. Surface-enhanced Raman scattering spectroscopy via gold nanostars. Journal of Raman Spectroscopy, 2009, 40 (1), pp. 86-91.

31. Green, M.; Liu, F.M. SERS substrates fabricated by island lithography: the silver/pyridine system. The Journal of Physical Chemistry B, 2003, 107 (47), pp. 13015-12021.

32. He, D.; Yao, Q.-F.; Wang, K.; Yu, S.-H. Large-scale synthesis of flexible free-standing SERS substrates with high sensitivity: electrospun PVA nanofibers embedded with controlled alignment of silver nanoparticles. ACS Nano, 2009, 3 (12), pp. 3993-4002.

33. Sharma, B.; Cardinal, M.F.; Kleinman, S.L.; Greeneltch, N.G.; Frontiera, R.R.; Blaber, M.G.; Schatz, G.C.; Van Duyne, R.P. High-performance SERS substrates: advances and challenges. MRS Bulletin, 2013, 38 (8), pp. 615-624.

34. Balachandran, Y.L.; Panarin, A.Y.; Khodasevich, I.A.; Terekhov, S.N.; Gutleb, A.C.; Girijaa, S. Environmentally Friendly Preparation of Gold and Silver Nanoparticles for Sers Applications Using Biopolymer Pectin. Journal of Applied Spectroscopy, 2015, 81 (6), pp. 962-968.

35. Suarasan, S.; Focsan, M.; Maniu, D.; Astilean, S. Gelatin–nanogold bioconjugates as effective plasmonic platforms for SERS detection and tagging. Colloids and Surfaces B: Biointerfaces, 2013, 103, pp. 475-481.

36. Potara, M.; Baia, M.; Farcau, C.; Astilean, S. Chitosan-coated anisotropic silvernanoparticles as a SERS substrate for single-molecule detection. Nanotechnology, 2012, 23 (5), pp. 1-10.

37. Stoddart, P.R.; Cadusch, P.J.; Boyce, T.M.; Erasmus, R.M.; Comins, J.D. Optical properties of chitin: surface-enhanced Raman scattering substrates based on antireflection structures on cicada wings. Nanotechnology, 2006, 17 (3), pp. 680-686.

38. Kean, T.; Thanou, M. Biodegradation, biodistribution and toxicity of chitosan. Advanced Drug Delivery Reviews, 2010, 62 (1), pp. 3-11.

39. Kumar-Krishnan, S.; Prokhorov, E.; Hernández-Iturriaga, M.; Mota-Morales, J.D.; Vázquez-Lepe, M.; Kovalenko, Y.; Sanchez, I.C.; Luna-Bárcenas, G. Chitosan/silver nanocomposites: synergistic antibacterial action of silver nanoparticles and silver ions. European Polymer Journal, 2015, 67, pp. 242-251.

40. Hakonen, A.; Andersson, P.O.; Schmidt, M.S.; Rindzevicius, T.; Käll, M. Explosive and chemical threat detection by surface-enhanced Raman scattering: A review. Analytica Chimica Acta, 2015, 893, pp. 1-13.

41. Jung, G.-B.; Kim, J.-H.; Burm, J.S.; Park, H.-K. Fabrication of chitosan-silver nanoparticle hybrid 3D porous structure as a SERS substrate for biomedical applications. Applied Surface Science, 2013, 273, pp. 179-183.

42. Li, J.; Zhang, G.; Wang, L.; Shen, A.; Hu, J. Simultaneous enzymatic and SERS properties of bifunctional chitosan-modified popcorn-like Au-Ag nanoparticles for high sensitive detection of melamine in milk powder. Talanta, 2015, 140, pp. 204-211.

43. Jones, S.; Pramanik, A.; Kanchanapally, R.; Nellore, B.P.V.; Begum, S.; Sweet, C.; Ray, P.C. Multifunctional three-dimensional chitosan/gold nanoparticle/graphene oxide architecture for separation, label-free SERS identification of pharmaceutical contaminants, and effective killing of superbugs. ACS Sustainable Chemistry & Engineering, 2017, 5 (8), pp. 7175-7187.

44. Sivanesan, A.; Kalaivani, G.; Fischer, A.; Stiba, K.; Leimkühler, S.; Weidinger, I.M. Complementary surface-enhanced resonance Raman spectroscopy biodetection of mixed protein solutions by chitosan- and silica-coated plasmon-tuned silver nanoparticles. Analytical Chemistry, 2012, 84 (13), pp. 5759-5764.

45. Ye, X.; Jin, L.; Caglayan, H.; Chen, J.; Xing, G.; Zheng, C.; Doan-Nguyen, V.; Kang, Y.; Enghetas, N.; Kagan, C.R.; Murray, C.B. Improved size-tunable synthesis of

monodisperse gold nanorods through the use of aromatic additives. ACS Nano, 2012, 6 (3), pp. 2804-2817.

46. Pérez-Mayen, L.; Oliva, J.; Torres-Castro, A.; De la Rosa, E. SERS substrates fabricated with star-like gold nanoparticles for zeptomole detection of analytes. Nanoscale, 2015, 7 (22), pp. 10249-10258.

47. Zhou, S.; Li, J.; Gilroy, K.D.; Tao, J.; Zhu, C.; Yang, X.; Sun, X.; Xia, Y. Facile Synthesis of Silver Nanocubes with Sharp Corners and Edges in an Aqueous Solution. ACS Nano, 2016, 10 (11), pp. 9861-9870.

48. Zhang, L.; Wang, B.; Zhu, G.; Zhou, X. Synthesis of silver nanowires as a SERS substrate for the detection of pesticide thiram. Spectrochimica Acta A, 2014, 133, pp. 411-416.

49. Sun, X.; Li, F.; Shen, G.; Huang, J.; Wang, X. Aptasensor based on the synergistic contributions of chitosan–gold nanoparticles, graphene–gold nanoparticles and multi-walled carbon nanotubes-cobalt phthalocyanine nanocomposites for kanamycin detection. Analyst, 2014, 139, pp. 299-308.

50. Xiang, C.; Li, R.; Adhikari, B.; She, Z.; Li, Y.; Kraatz, H.-B. Sensitive electrochemical detection of *Salmonella* with chitosan–gold nanoparticles composite film. Talanta, 2015, 140, pp. 122-127.

51. Venkatesham, M.; Ayodhya, D.; Madhusudhan, A.; Babu, N.V.; Veerabhadram, G. A novel green one-step synthesis of silver nanoparticles using chitosan: catalytic activity and antimicrobial studies. Applied Nanoscience, 2014, 4 (1), pp. 113-119.

52. Li, D.; Lv, D.Y.; Zhu, Q.X.; Li, H.; Chen, H.; Wu, M.M.; Chai, Y.F.; Lu, F. Chromatographic separation and detection of contaminants from whole milk powder using a chitosan-modified silver nanoparticles surface-enhanced Raman scattering device. Food Chemistry, 2017, 224, pp. 382-389.

53. Nhung, T.T.; Bu, Y.; Lee, S.-W. Facile synthesis of chitosan-mediated gold nanoflowers as surface-enhanced Raman scattering (SERS) substrates. Journal of Crystal Growth, 2013, 373, pp. 132-137.

54. Yang, K.-H.; Chang, C.-M. Using a photochemical method and chitosan to prepare surface-enhanced Raman scattering–active silver nanoparticles. Analytica Chimica Acta, 2012, 729, pp. 1-6.

55. Oliveira, D.G.; Peixoto, L.P.F.; Sánchez-Cortés, S.; Andrade, G.F.S. Chitosan-based improved stability of gold nanoparticles for the study of adsorption of dyes using SERS. Vibrational Spectroscopy, 2016, 87, pp. 8-13.

56. Ou, K.-L.; Hsu, T.-C.; Liu, Y.-C.; Yang, K.-H.; Sun, W.-H. Strategy on effective detection of acetaldehydes by using surface-enhanced Raman scattering-active

chitosan-capped nanostructured Au. Journal of Electroanalytical Chemistry, 2013, 702, pp. 66-71.

57. Wang, W.; Yang, C.; Cui, X.Q.; Bao, Q.L.; Li, C.M. Droplet microfluidic preparation of au nanoparticles-coated chitosan microbeads for flow-through surface-enhanced Raman scattering detection. Microfluidics Nanofluidics, 2010, 9 (6), pp.1175-1183.

58. He, J.; Li, G.; Hu, Y. Aptamer Recognition Induced Target-Bridged Strategy for Proteins Detection Based on Magnetic Chitosan and Silver/Chitosan Nanoparticles Using Surface-Enhanced Raman Spectroscopy. Analytical Chemistry, 2015, 87 (21), pp. 11039-11047.

59. Lim, J.-W.; Kang, I.J. Fabrication of Chitosan-gold Nanocomposites Combined with Optical Fiber as SERS Substrates to Detect Dopamine Molecules. Bulletin of the Korean Chemical Society Soc, 2014, 35 (1), pp. 25-29.

60. Potara, M.; Boca, S.; Licarete, E.; Damert, A.; Alupei, M.-C.; Chiriac, M.T.; Popescu, O.; Schmidt, U.; Astilean, S. Chitosan-coated triangular silver nanoparticles as a novel class of biocompatible, highly sensitive plasmonic platforms for intracellular SERS sensing and imaging. Nanoscale, 2013, 5 (13), pp. 6013-6022.

61. Potara, M.; Gabudean, A.M.; Astilean, S. Solution-phase, dual LSPR-SERS plasmonic sensors of high sensitivity and stability based on chitosan-coated anisotropic silver nanoparticles. Journal of Materials Chemistry, 2011, 21 (11), pp. 3625-3633.

62. Lim, J.W.; Kang, I.-J. Chitosan-gold Nano Composite for Dopamine Analysis using Raman Scattering. Bulletin of the Korean Chemical Society, 2013, 34 (1), 237-242.

63. De Barros, E.; Lopes, E.C.; Santos, C.; Aparecido, F.; Odone, I. Fast detection of paracetamol on a gold nanoparticle–chitosan substrate by SERS. Analytical Methods, 2014, 6, pp. 3564-3568.

64. Prikhozhdenko, E.S.; Lengert, E.V.; Parakhonskiy, B.V.; Gorin, D.A.; Sukhorukov, G.B.; Yashchenok, A.M. Biocompatible Chitosan Nanofibers Functionalizedwith Silver Nanoparticles for SERS Based Detection. Acta Physica Polonica A, 2016, 129 (2), pp. 247-249.

65. Zhang, G.; Li, J.; Shen, A.; Hu, J. Synthesis of size-tunable chitosan encapsulated gold–silver nanoflowers and their application in SERS imaging of living cells. Physical Chemistry Chemical Physics, 2015, 17 (33), pp. 21261-21267.

66. Lim, J.-W.; Kang, I.-J. Fabrication of Chitosan-Gold Nanoshells for γ-Aminobutyric Acid Detection as a Surface-enhanced Raman Scattering Substrate. Bulletin of the Korean Chemical Society, 2015, 36, pp. 672-677.

67. De Barros, E.; Aparecido, F.; Odone, I. Facile synthesis of the dendritic structure of silver nanoparticles–chitosan and its application as an effective SERS substrate. New Journal of Chemistry, 2014, 38 (11), pp. 5369-5375.

68. Dos Santos, D.S.; Goulet, P.J.; Pieczonka, N.P.W.; Oliveira, O.N.; Aroca, R.F. Gold Nanoparticle Embedded, Self-Sustained Chitosan Films as Substrates for Surface-Enhanced Raman Scattering. Langmuir, 2004, 20, pp. 10273-10277.

69. Potara, M.; Maniu, D.; Astilean, S. The synthesis of biocompatible and SERS-active gold nanoparticles using chitosan. Nanotechnology, 2009, 20 (31), pp. 1-7.

70. Chen, K.; Shen, Z.; Luo, J.; Wang, X.; Sun, R. Quaternized chitosan/silver nanoparticles composite as a SERS substrate for detecting tricyclazole and Sudan I. Applied Surface Science, 2015, 351, pp. 466-473.

71. Xu, D.; Gu, J.; Wang, W.; Yu, X.; Xi, K.; Jia, X. Development of chitosan-coated goldnanoflowers as SERS-active probes. Nanotechnology, 2010, 21 (37), pp. 1-8

72. Luo, X.L.; Buckhout-White, S.; Bentley, W.E.; Rubloff, G.W. Biofabrication of chitosan–silver composite SERS substrates enabling quantification of adenine by a spectroscopic shift. Biofabrication, 2011, 3 (3), pp. 034108-034116.

73. Severyukhina, A.N.; Parakhonskiy, B.V.; Prikhozhdenko, E.S.; Gorin, D.A.; Sukhorukov, G.B.; Möhwald, H.; Yashchenok, A.M. Nanoplasmonic Chitosan Nanofibers as Effective SERS Substrate for Detection of Small Molecules. ACS Applied Materials & Interfaces, 2015, 7 (28), pp. 15466-15473.

74. Prikhozhdenko, E.S.; Atkin, V.S.; Parakhonskiy, B.V.; Rybkin, I.A.; Lapanje, A.; Sukhorukov, G.B.; Gorin, D.A.; Yashchenok, A.M. New post-processing method of preparing nanofibrous SERS substrates with a high density of silver nanoparticles. RSC Advances, 2016, 6, pp. 84505-84511.

75. Wang, C.; Wong, K.W.; Wang, Q.; Zhou, Y.; Tang, C.; Fan, M.; Mei, J.; Lau, W.-M. Silver-nanoparticles-loaded chitosan foam as a flexible SERS substrate for active collecting analytes from both solid surface and solution. Talanta, 2019, 191, pp. 241-247.

76. López, I.; Vázquez, A.; Hernández-Padrón, G.H.; Gómez, I. Electrophoretic deposition (EPD) of silver nanoparticles and their application as surface-enhanced Raman scattering (SERS) substrates. Applied Surface Science, 2013, 280, pp. 715-719.

77. López, I.; Ceballos, M.; Gómez, I. (2016, April). Exciton-Plasmon Interactions between CdS Quantum Dots and Noble Metal Nanospheres in Aqueous Dispersion. In World Congress on Recent Advances in Nanotechnology (RAN'16), Prague, Czech Republic.

78. Pillai, Z.S.; Kamat, P.V. What Factors Control the Size and Shape of Silver Nanoparticles in the Citrate Ion Reduction Method? Journal of Physical Chemistry B, 2004, 108 (3), pp. 945-951.

79. Sun, Y.; Gates, B.; Mayers, B.; Xia, Y. Crystalline Silver Nanowires by Soft Solution Processing. Nano Letters, 2002, 2 (2), pp. 165-168.

80. Liang, E.J.; Engert, C.; Kiefer, W. Surface-enhanced Raman scattering of halide ions, pyridine and crystal violet on colloidal silver with near-infrared excitation: low-wavenumber vibrational modes. Vibrational Spectroscopy, 1995, 8 (3), pp. 435-444.

APPENDIX

APPENDIX

ELECTROCHEMICAL SURFACE-ENHANCED RAMAN SPECTROSCOPY (EC-SERS)

APPENDIX

ELECTROCHEMICAL SURFACE-ENHANCED RAMAN SPECTROSCOPY (EC-SERS)

Since its development in 1974, the SERS technique has grown remarkably and a wide variety of substrates is now available for their purchase and use; however, SERS can be easily coupled with other techniques to further enhance its sensitivity and performance. Among the modifications of this technique, EC-SERS offers advantages such as: observing the conformational change in the analyte molecules, orientation of the probe molecule, and thus leading to higher intensities, studying catalytic processes, detecting samples in biological-like conditions, analyzing the electrochemical stability of a given molecule, increasing the adsorption of analytes that interact with the metal surface by physisorption [A1-A4].

To perform an EC-SERS analysis, an electric potential must be applied on the substrate as the Raman spectrometer collects the vibrational information of molecules on the surface of the substrate. The equipment used is usually an electrochemical cell containing working, counter, and reference electrodes immersed in a suitable electrolyte such as NaF or KCl. As shown in Fig. A1; a potentiostat/galvanostat instrument allows control in the applied potential, as well as the electrochemical characterization of the substrate after the EC-SERS analysis. The use of screen-printed electrodes (SPE) gained popularity due to their low cost, reproducibility and customize capability. This kind of electrodes are usually made of a polymer and contain the working, counter and reference electrodes in a small area, simplifying the system. Although the working electrode is

usually a carbon, Ag or Au electrode, it can be modified by placing a film of a SERS-active material, making this kind of electrodes suitable substrates for EC-SERS [A5-A9].

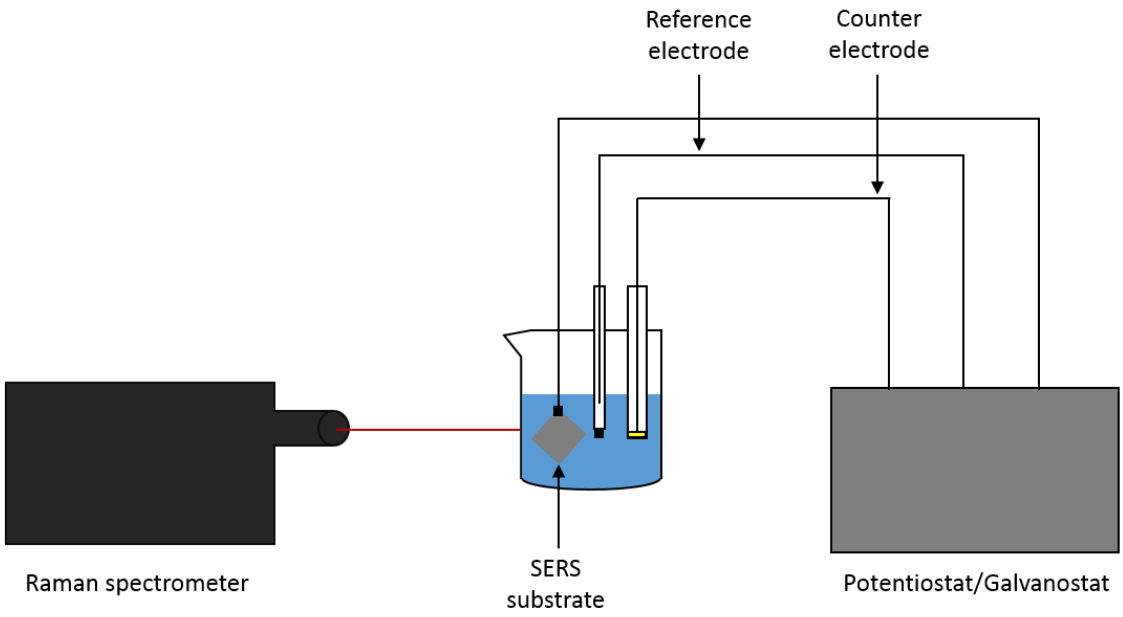

Fig. A1. EC-SERS set up required for a regular analysis.

Selecting the EC-SERS substrate that best suits the need of detecting a specific type of analyte is often hard, parameters as the required potential, the molecule-substrate affinity, and the expected sensitivity must be defined to choose a substrate. Although each substrate is different, those composed of Ag nanomaterials offer higher Raman intensities than those of Au; however, when a positive potential is required, a Au-based substrate is suggested due to its electrochemical stability at negative and positive potentials, whereas the Ag materials oxidize at a low positive voltage. On the other hand, Au-based substrates usually present higher biocompatibility that allows the determination of biological analytes of high interest; however, their lowest concentration that can be determined is usually not as low as the one that can be observed using a Ag nanoparticle substrate.

EC-SERS has been used to develop different studies such as the interaction between oligomers, protofibrils, and fibrils with a biomimetic bilayer lipid membrane [A10]; detection of quinacridone quinone using a Cu working electrode and ionic liquids as electrolytes [A11]; *in situ* study of the intermediate species formed during the electrochemical reduction of benzyl chloride [A12]; determination of levoflaxin in synthetic urine for point-of-care (POC) diagnosis [A13]; the detection of aminoglutethimide [A14]; among other studies.

A.1. Materials and methods

In order to study the behavior of the previously prepared nanoparticle dispersions as EC-SERS substrates, commercial carbon screen-printed electrodes (Model RRPE1002C, Pine Research) were modified by coating the carbon working electrode with a nanoparticle paste. In a regular modification process, 5 μL of the paste were added onto the working electrode, covering all of the active area and letting it dry. This process was performed three times with the AgNS, AuNS, and AuNR pastes; only one coat was used in the case of the AgNC.

After the substrates modification, 5 μL of the analyte (1 mM *p*-ATP in this case) were added to the modified working electrode and let dry. The substrates were added to an EC-SERS vial containing a lid. This lid can hold the substrates and also is connected to a potentiostat/galvanostat (Pine Research WaveNow Potentiostat/Galvanostat System). With the substrate set in the vial, an electrolyte solution must be added to prevent electrical issues, in this case, 0.1 M NaF was added until the volume covered the substrate active

area. With the electrolyte in the system, a current was applied to the electrode and maintained for time enough to allow the recording of a Raman spectrum. In order to evaluate the effect of different voltages, cathodic and anodic experiments were performed, in which the former consist in applying an electric potential between 0 and –1 V at 100 mV steps; on the other hand, the anodic experiments consisted on applying a voltage between –1 V and 0 V at 100 mV steps. A Raman spectra was recorded at each step for all of the substrates. All potentials are reported versus Ag/AgCl, and the Raman spectrometer was a DeltaNu Advantage 785.

FE-SEM analysis of the modified SPE's active area were performed in a Tescan Mira 3 microscope at 20 kV and a secondary electron detector.

A.2. Results and discussion

The modification of the SPEs with the different nanoparticle pastes can be observed in Fig. A2. In this image, the carbon electrode (black color) changes its color in a dependent way with the nanoparticle dispersion used.

In Fig. A3, the FE-SEM analysis of the modified electrodes active area is presented. In this the case of the AgNS-modified substrate, an irregular surface can be observed; however, it is possible that the Raman intensities of the molecule vibrational modes will be enhanced due to the roughness of this substrate. On the other hand, Fig. A3(b) shows the surface of the SPE modified with AgNC. This substrate was modified with only one coat of particles due to the low volume of AgNC paste obtained by the followed method. The micrograph shows an agglomerate of cube-like particles and nanorods, similar to the

particles obtained and previously characterized; however, these particles merge and produce a larger structure formed by rounded cubes.

The AuNS coating deposited onto one of the SPE is presented in Fig. A3(c), and it shows a matrix of irregular particles. Once again, this micrograph shows a roughened surface that can be beneficial to achieve high SERS enhancements. Similarly to the AgNC substrate, the electrode modified with AuNR shows some of the nanorods; nevertheless, these particles are in a matrix of Au particle agglomerates. These results show that the morphology of the particles becomes less defined as more layers are deposited.

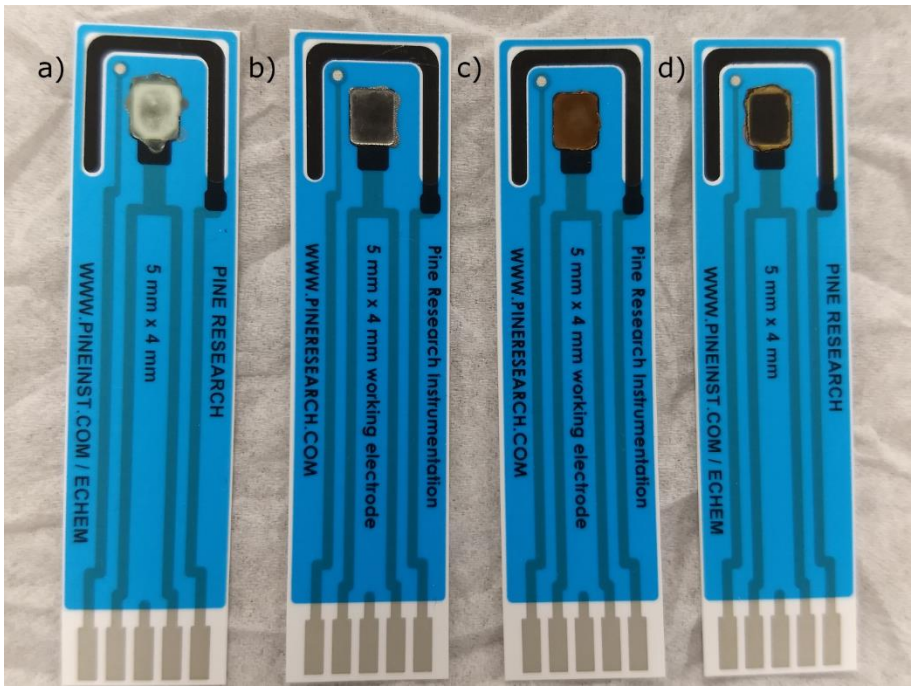

Fig. A2. EC-SERS substrates modified with a) AgNS, b) AgNC, c) AuNS, and d) AuNR.

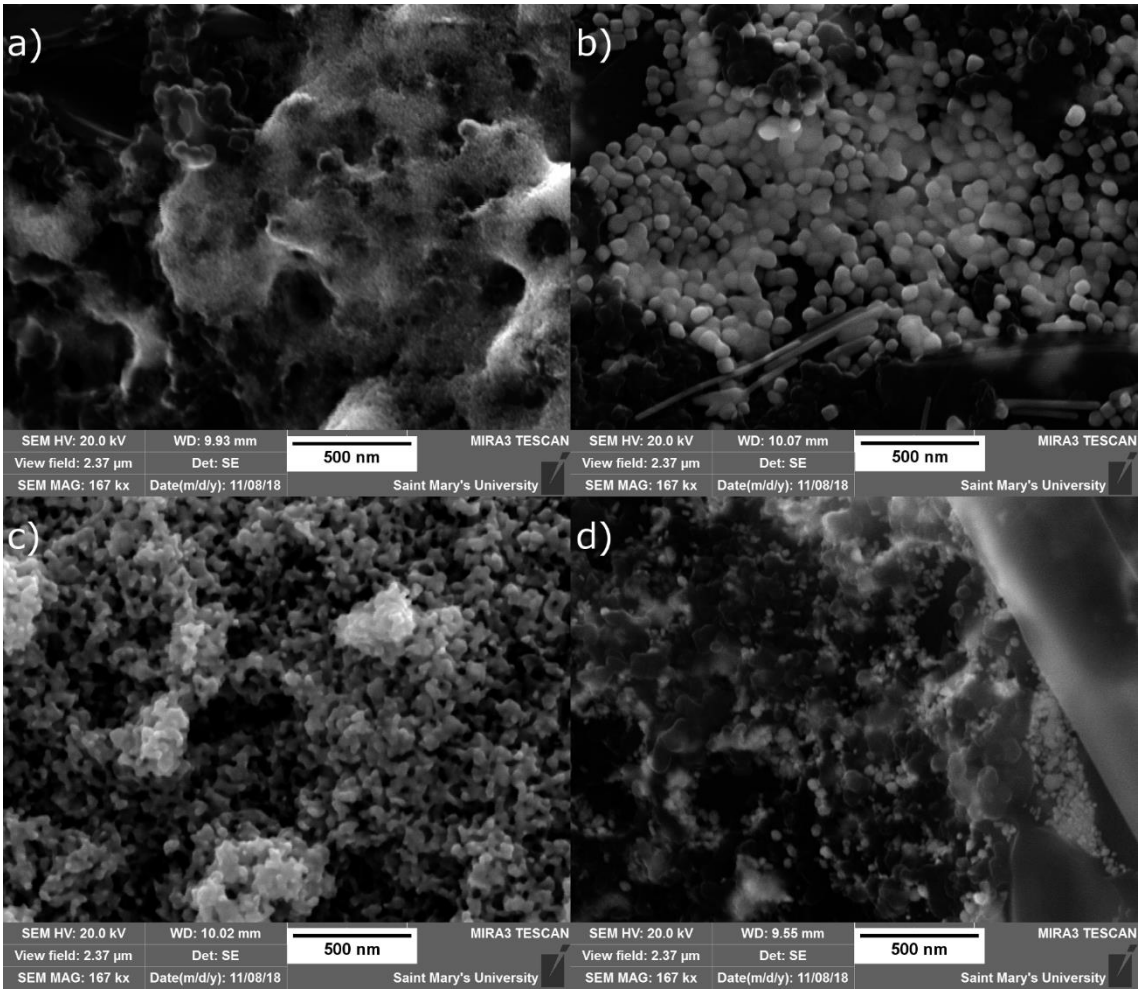

Fig. A3. FE-SEM of the EC-SERS modified substrates: a) AgNS, b) AgNC, c) AuNS, and d) AuNR.

Fig. A4 shows the Raman spectra recorded for the four kinds of substrates using 1 mM *p*-ATP as probe molecule in air conditions; this is the analysis performed before the addition of the electrolyte and the applied voltage. These results show that the substrates based on Ag nanoparticles produce spectra with more defined bands. In can also be observed that the AgNS electrode shows the highest Raman intensity enhancements, while the AuNR substrate shows the lowest. The intensities reached by the latter substrate are not smaller than the background intensities and thus, the bands are poorly defined.

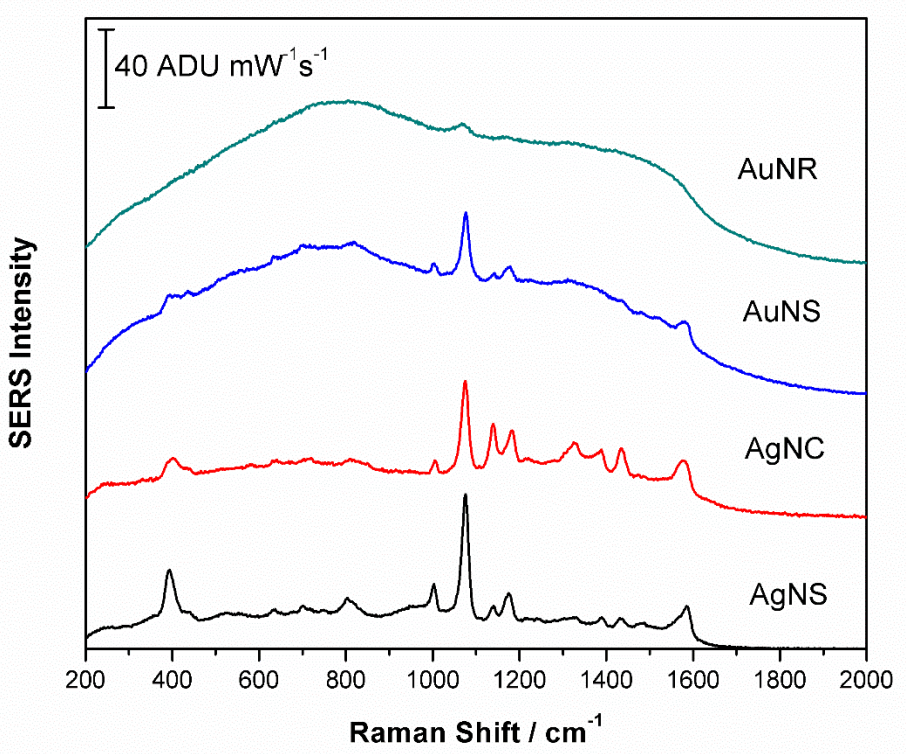

Fig. A4. SERS spectra recorded by the EC-SERS modified substrates at air conditions and using 1 mM *p*-ATP.

EC-SERS spectra were recorded with the four modified SPEs and the results are presented in Fig. A5, A6, A7, and A8, which are listed for AgNS, AgNC, AuNS, and AuNR, respectively.

In these spectra, it can be observed the decrease of a vibrational mode recorded at 1140 cm^{-1}, which corresponds to a different molecule: 4,4'-dimercaptobenzene (DMAB). This molecule is produced due to the catalyzed reaction that occur at the metallic substrate surface, in which energy transfer from the plasmonic heating is transferred to the *p*-ATP molecules, where O_2 acts as an electron acceptor, producing the deprotonation agent O_2^-. Then, the deprotonated moiety interacts with another deprotonated *p*-ATP molecule, leading to a NH–NH bond. This process occurs twice, and thus, the final product presents

a N=N bond, whose vibrational modes can be observed close to 1388 and 1420 cm^{-1} in Raman spectroscopy [A15]. However, the voltage applied during the EC-SERS analysis can produce the reverse reaction, decreasing the DMAB bands, and increasing the intensity of the *p*-ATP vibrational modes. This voltage is close to –0.9 V for the AgNS and AgNC substrates, near –0.8 V for AuNS, and higher than –1.0 V for AuNR. These voltages offer the best spectra that can be obtained using these substrates and this Raman probe, and it can be used during a cathodic or an anodic experiment.

Similarly to the experiments presented previously in this work, the enhancement obtained by these substrates can be compared. The highest intensities were reached by the AgNC-modified electrodes at the cathodic experiment, followed by the AgNS substrates. The Au-based SPEs show the lowest intensities of the study, and although the lowest enhancement was reached by the AuNR particles, these substrates show less background intensities and thus their spectra are better defined than those obtained using AuNS.

Even though the intensities obtained by the Au substrates were low, these electrodes offer some advantages against the Ag ones. An example of this, is the voltage range that can be used, allowing the use of Au-based electrodes for positive potentials; also, the stability of this kind of particles is often higher than those made of Ag. Due to this and more advantages, these substrates can be widely used for the analysis of a variety of biological and chemical samples.

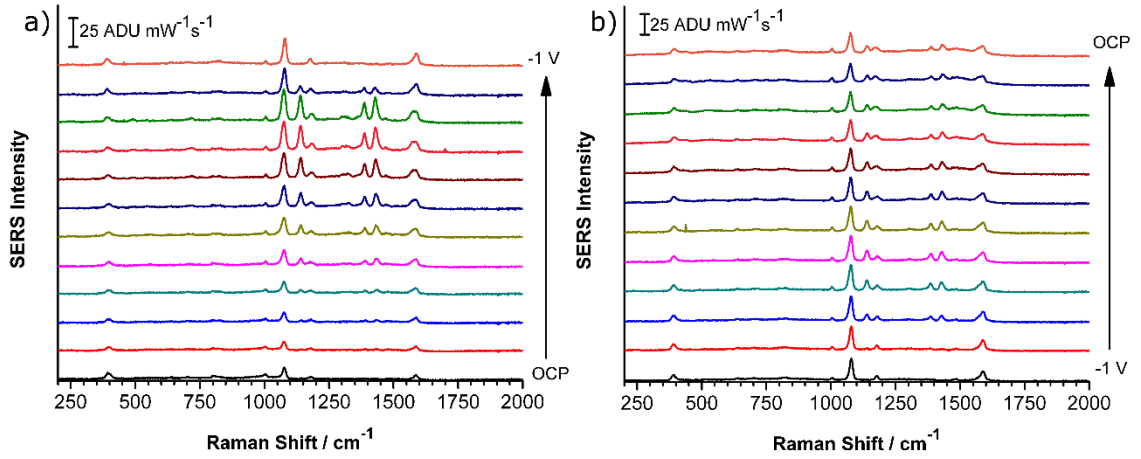

Fig. A5. EC-SERS spectra of 1 mM *p*-ATP on AgNS-modified electrodes; a) cathodic, and b) anodic experiments.

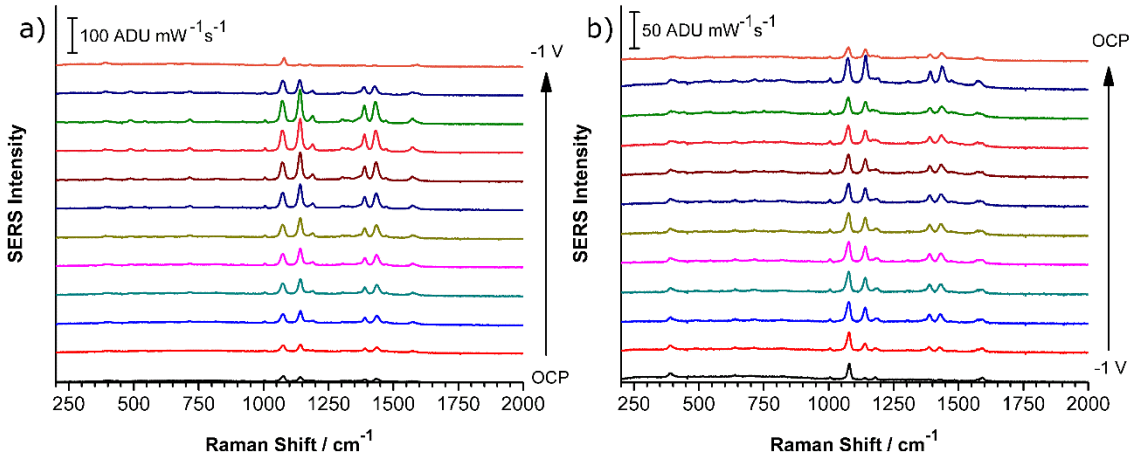

Fig. A6. EC-SERS spectra of 1 mM *p*-ATP on AgNC-modified electrodes; a) cathodic, and b) anodic experiments.

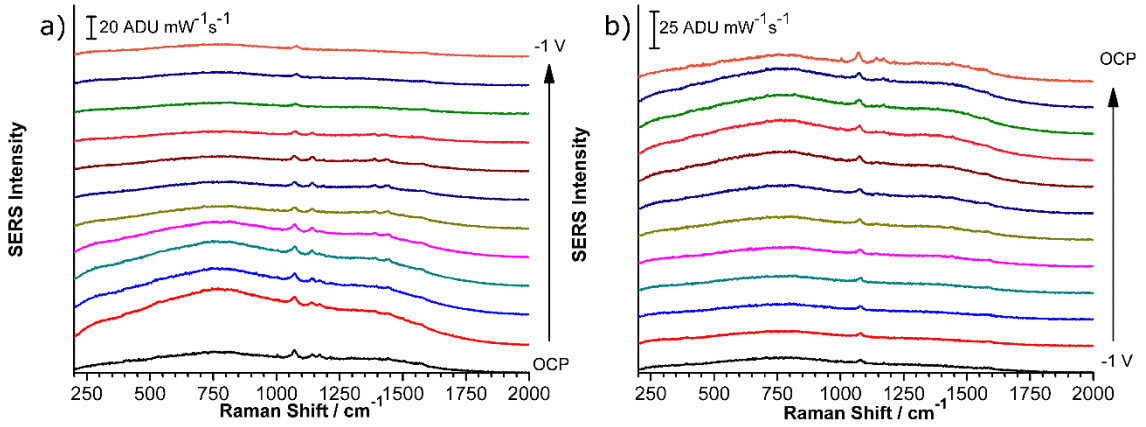

Fig. A7. EC-SERS spectra of 1 mM *p*-ATP on AuNS-modified electrodes; a) cathodic, and b) anodic experiments.

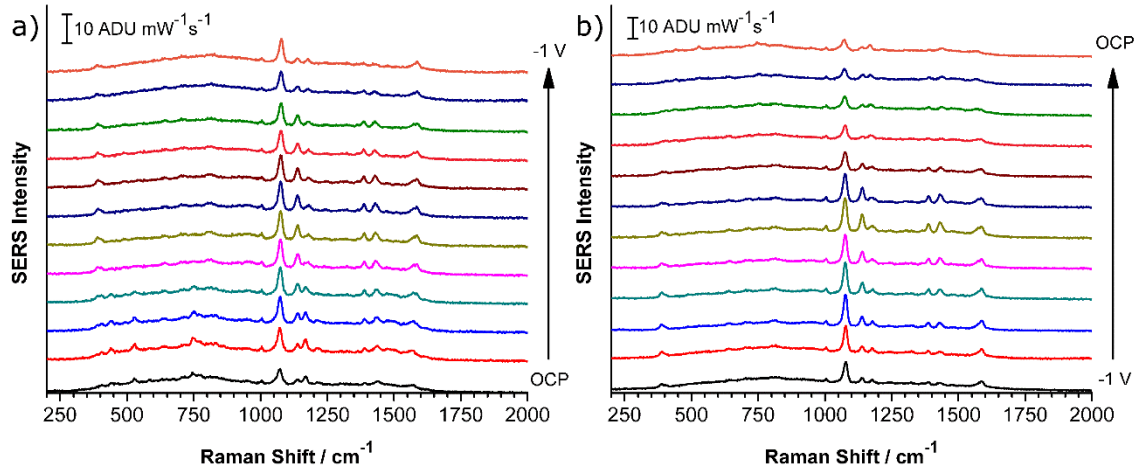

Fig. A8. EC-SERS spectra of 1 mM *p*-ATP on AuNR-modified electrodes; a) cathodic, and b) anodic experiments.

References

A1. Wu, D.-Y.; Li, J.-F.; Ren, B.; Tian, Z.-Q. Electrochemical surface-enhanced Raman spectroscopy of nanostructures. Chemical Society Reviews, 2008, 37 (5), pp. 1025-1041.

A2. Robinson, A.M.; Harroun, S.G.; Bergman, J.; Brosseau, C.L. Portable Electrochemical Surface-Enhanced Raman Spectroscopy System for Routine Spectroelectrochemical Analysis. Analytical Chemistry, 2012, 84 (3), pp. 1760-1764.

A3. Karaballi, R.A.; Nel, A.; Krishnan, S.; Blackburn, J.; Brosseau, C.L. Development of an electrochemical surface-enhanced Raman spectroscopy (EC-SERS) aptasensor for direct detection of DNA hybridization. Physical Chemistry Chemical Physics, 2015, 17 (33), pp. 21356-21363.

A4. Dendisová, M.; Nemecková, Z.; Clupek, M.; Prokopec, V. EC-SERS study of phenolic acids sorption behavior on Au, Ag and Cu substrates – Effect of applied potential and metal used. Applied Surface Science, 2019, 470, pp. 716-723.

A5. Goodall, B.L.; Robinson, A.M.; Brosseau, C.L. Electrochemical-surface enhanced Raman spectroscopy (E-SERS) of uric acid: a potential rapid diagnostic method for early preeclampsia detection. Physical Chemistry Chemical Physics, 2013, 15 (5), pp. 1382-1388.

A6. Martín-Yerga, D.; Pérez-Junquera, A.; González-García, M.B.; Perales-Rondon, J.V.; Heras, A.; Colina, A.; Hernández-Santos, D.; Fanjul-Bolado, P. Quantitative Raman spectroelectrochemistry using silver screen-printed electrodes. Electrochimica Acta, 2018, 264, pp. 183-190.

A7. Clarke, O.J.R.; St. Marie, G.J.; Brosseau, C.L. Evaluation of an Electrodeposited Bimetallic Cu/Ag Nanostructured Screen Printed Electrode for Electrochemical Surface-Enhanced Raman Spectroscopy (EC-SERS) Investigations. Journal of the Electrochemical Society, 2017, 164 (5), pp B3091-B3095.

A8. Zhu, Z.; Yoshikawa, H.; Saito, M.; Fan, B.; Tamiya, E. Fabrication of Surface-enhanced Raman Spectroscopy (SERS) – Active Electrodes by Silver Sputtering Deposition for Electrochemical SERS Analysis. Electroanalysis, 2018, 30, pp. 1432-1437.

A9. Teng, Y.; Ding, G.; Liu, W.; Liu, J.; Nie, Y.; Li, P. Electrodeposition of dendritic gold/silver nanaoparticles on disposable screen-printed carbon electrode and its application of 4-mercaptopyridine in in situ electrochemical surface-enhanced Raman scattering. Surface and Interface Analysis, 2016, 48, pp. 990-994.

A10. Karaballi, R.A.; Merchant, S.; Power, S.R.; Brosseau, C.L. Electrochemical surface-enhanced Raman spectroscopy (EC-SERS) study of the interaction between protein aggregates and biomimetic membranes. Physical Chemistry Chemical Physics, 2018, 6 (20), pp. 4513-4526.

A11. del Puerto, E.; Cuesta, A.; Sanchez-Cortes, S.; García-Ramos, J.V.; Domingo, C. Electrochemical SERS study on a copper electrode of the insoluble organic pigment quinacridone quinone using ionic liquids (BMIMCl and TBAN) as dispersing agents. Analyst, 2013, 16 (138), pp. 4670-4676.

A12. Wang, A.; Huang, Y.-F.; Sur, U.K.; Wu, D.-Y.; Ren, B.; Rondinini, S.; Amatore, C.; Tian, Z.-Q. *In Situ* Identification of Intermediates of Benzyl Chloride Reduction

at a Silver Electrode by SERS Coupled with DFT Calculations. Journal of the American Chemical Society, 2010, 132 (28), pp. 9534-9536.

A13. Bindesri, S.D.; Alhatab, D.S.; Brosseau, C.L. Development of an electrochemical surface-enhanced Raman spectroscopy (EC-SERS) fabric-based plasmonic sensor for point-of-care diagnostics. Analyst, 2018, 17 (143), pp. 4128-4135.

A14. Zhu, Z.; Espulgar, W.V.; Yoshikawa, H.; Saito, M.; Fan, B.; Dou, X.; Tamiya, E. Electrochemically Modulated Surface-Enhanced Raman Spectra of Aminoglutethimide (AGI) on a Ag-Sputtered Electrode. Bulletin of the Chemical Society of Japan, 2018, 91 (11).

A15. Huang, Y.-F.; Wu, D.-Y.; Zhu, H.-P.; Zhao, L.-H.; Liu, G.-K.; Ren, B.; Tian, Z.-Q. Surface-enhanced Raman spectroscopic study of *p*-aminothiophenol. Physical Chemistry Chemical Physics, 2012, 24 (14), pp. 8485-8497.